Many-Body Singlet Prepared by a Central-Spin Qubit

Leon Zaporski,[1,‡] Stijn R. de Wit,[1,2,‡] Takuya Isogawa,[1] Martin Hayhurst Appel,[1] Claire Le Gall,[1] Mete Atatüre,[1,*] and Dorian A. Gangloff[3,†]

[1] *Cavendish Laboratory, University of Cambridge, JJ Thomson Avenue, Cambridge CB3 0HE, United Kingdom*
[2] *MESA+ Institute for Nanotechnology, University of Twente, The Netherlands*
[3] *Department of Engineering Science, University of Oxford, Parks Road, Oxford OX1 3PJ, United Kingdom*

(Received 24 January 2023; accepted 20 October 2023; published 14 December 2023)

Controllable quantum many-body systems are platforms for fundamental investigations into the nature of entanglement and promise to deliver computational speed-up for a broad class of algorithms and simulations. In particular, engineering entanglement within a dense spin ensemble can turn it into a robust quantum memory or a computational platform. Recent experimental progress in dense central-spin systems motivates the design of algorithms that use a central-spin qubit as a convenient proxy for the ensemble. Here we propose a protocol that uses a central spin to initialize two dense spin ensembles into a pure antipolarized state and from there creates a many-body entangled state—a singlet—from the combined ensemble. We quantify the protocol performance for multiple material platforms and show that it can be implemented even in the presence of realistic levels of decoherence and diffusion. Our protocol introduces an algorithmic approach to the preparation of a known many-body state and to entanglement engineering in a dense spin ensemble, which can be extended towards a broad class of collective quantum states.

DOI: 10.1103/PRXQuantum.4.040343

I. INTRODUCTION

Controlling quantum properties in many-particle systems, whether for technological advantage or foundational studies, can be reduced to controlling the relative participation and phase of the system's eigenstates. In most cases, this leads to entanglement amongst the system's particles [1]. The initialization of a quantum system to a pure state is a necessary starting point from which to engineer entanglement via unitary dynamics [2]. Initialization through traditional cooling techniques brings a quantum system in contact with a bath whose temperature is below that of the system's characteristic energy scale, bringing the target system to its ground state [3]. An equivalent picture exists for driven systems, where directionality within an energy hierarchy of dressed states can bring the system to an effective ground state of the dressed system [4]. The latter approach is more versatile as it allows the design of tailored ground states. Crucially, it also requires access to the degree of freedom one intends to cool. Versions of this approach appear in driven-dissipative state preparations of photonic systems [5,6], diamond color centers [7–9], epitaxial quantum dots [10,11], and atomic ensembles [12,13].

Central-spin systems, typically consisting of a single electronic spin coupled to an ensemble of nuclear spins [14] have been a particularly potent testing ground for the active approaches to state preparation [15,16]. Firstly, this is by necessity: nuclear-spin energy scales make ground-state preparation well beyond the reach of modern refrigeration techniques. Secondly, the one-to-all coupling of the central-spin qubit to an ensemble of spins yields a convenient proxy for the ensemble spins [17]. In the few-spin regime of diamond color centers or rare-earth ions, dynamic nuclear polarization can initialize a set of proximal spins to a high-purity polarized state [18]. This is then the starting point for qubit storage in an ensemble excitation [19], two-body singlet engineering [20], or spin-by-spin quantum computation [21].

In the limit of dense ensembles, the constituent spins are indistinguishable when interacting with the central spin. Entanglement is then readily generated and measured by controlling the central spin's dynamics [17,22,23]. Collective states of the ensemble become natural targets of a driven purification technique [16]. In addition, an effective all-to-all coupling mediated by the central spin [24] leads to a highly correlated behavior of the ensemble that, in

*Corresponding author. ma424@cam.ac.uk
†Corresponding author. dag50@cam.ac.uk
‡These authors contributed equally.

principle, can be harnessed for state engineering. Despite the absence of individual spin control, the dense systems of interest [15,25,26] operate in a truly many-body regime of 10^4 to 10^6 interacting ensemble spins—far exceeding the number of physical qubits present in near-term quantum simulators [27,28]. In several ways, this is analogous to cavity quantum electrodynamics with ensembles of atoms where a single cavity photon is a central boson capable of carving entangled collective states of atomic spins [29–31].

A many-body singlet is a superposition of ensemble spins with zero angular momentum [32]. The singlet state is a hyperfine vacuum and renders the bath invisible to the central spin, protecting the latter from interacting with its environment [7,33,34]—a decoherence-free subspace for the central-spin qubit. Owing to destructive interference between pairs of ensemble spins, the ensemble is also protected from noise whose length scale is larger than the system size. This makes it a particularly useful and readily detectable first target state to prepare in a central-spin system. Furthermore, many-body singlet preparation offers insights into the evolution of entanglement under slower intrabath interactions, as well as anomalous spin diffusion at longer time scales [35].

To date, state engineering efforts in dense central-spin systems remain confined to tuning the mean field degrees of freedom, such as ensemble polarization and its fluctuations [16,22,36,37], and classical correlations amongst ensemble spins [23]. A degree of purification has been achieved via polarization of 80% through optical techniques [38] and nearly 50% via central-spin control [23]—such approaches proving to be generally challenging due to a dependence of the central-spin transition frequency on the polarization of the bath. Meanwhile, stabilizing the ensemble polarization via the central spin [16] can approach the quantum limit of polarization stability. Despite these efforts, the resulting nuclear states remain highly mixed, featuring little interparticle phase coherence. A degree of quantum correlation among spins was observed when probing a partially polarized ensemble via the central spin [23], which suggested the possibility of purification via reduced total angular momentum states, so-called dark states [39]. Theoretical proposals to engineer the state of dense central-spin systems have focused on dissipative phase transitions [4], or quantum memory [10,39] and spin squeezing schemes [40] relying on fully polarized initial states. A protocol for direct control over the ensemble's interparticle phase, allowing for purification and entanglement engineering at low total ensemble polarization, is still missing.

In this work, we use a simple and realistic form of symmetry breaking to gain control over an ensemble's interparticle phase. Leveraging this control, we propose a three-stage state engineering protocol that utilizes the effective interaction between two distinct spin species, naturally present in real physical systems [15,25,26], and proceeds via control of the central spin exclusively. The first stage of the protocol locks the total polarization of the system to zero [16]. The second stage initializes the two spin species to an antipolarized state with near-unit purity. The third stage involves a sequence of unitary gates that drives the system into a many-body singlet via phase engineering. Having in mind a near-term experimental realization, we quantify the protocol robustness as a function of model parameters and identify candidate physical platforms in which it could be successfully implemented.

II. THEORY AND RESULTS

A. Symmetry and the total angular momentum representation

Central-spin systems feature high-dimensional Hilbert spaces. In the dense limit, the central spin's interaction with the ensemble does not distinguish individual spins. This leads to collective symmetries and corresponding constants of motion, which we focus on here.

In this simplest scenario of a perfectly homogeneous spin bath [see Fig. 1(a)], a general system Hamiltonian is unchanged under the reordering of ensemble spin indices. Such invariance is the highest symmetry that a spin bath can exhibit, and it results in the emergence of a constant of motion that dictates the rate of collective dynamics, as in Dicke super-radiance [41]. Within the bath of spin-1/2 particles, this constant is identical to the magnitude of the total angular momentum, I, directly related to the eigenvalue of

$$\left(\sum_{k=1}^{N}\mathbf{i}_k\right)^2 \equiv \mathbf{I}^2, \tag{1}$$

where $\mathbf{i}_k$ is the single-spin operator of the kth spin in the ensemble and N is the total number of ensemble spins. Ensembles of higher-spin particles, such as spin 3/2, can be described by equivalent, albeit more numerous, constants of motion.

Under this symmetry, coupling to the central spin cannot change the magnitude of the total angular momentum, only the polarization, and coherent control over the ensemble is thereby limited. In particular, efforts to prepare a many-body singlet ($I = 0$) are futile and the ensemble dynamics is governed by thermally (with $\beta \sim 0$) occupied states of I, dominated by the highest degeneracy states near $I \sim \sqrt{N}$.

We propose making use of the simplest form of reduced symmetry to gain control: breaking the system into two distinguishable but equally abundant ensembles [see Fig. 1(b)], which we call species. The groups of spins of the same species are characterized by their individual total angular momenta: $\mathbf{I}_1$ and $\mathbf{I}_2$. Their magnitudes, I_1 and I_2, become the new constants of motion (over long timescales governed by the weak processes that break the

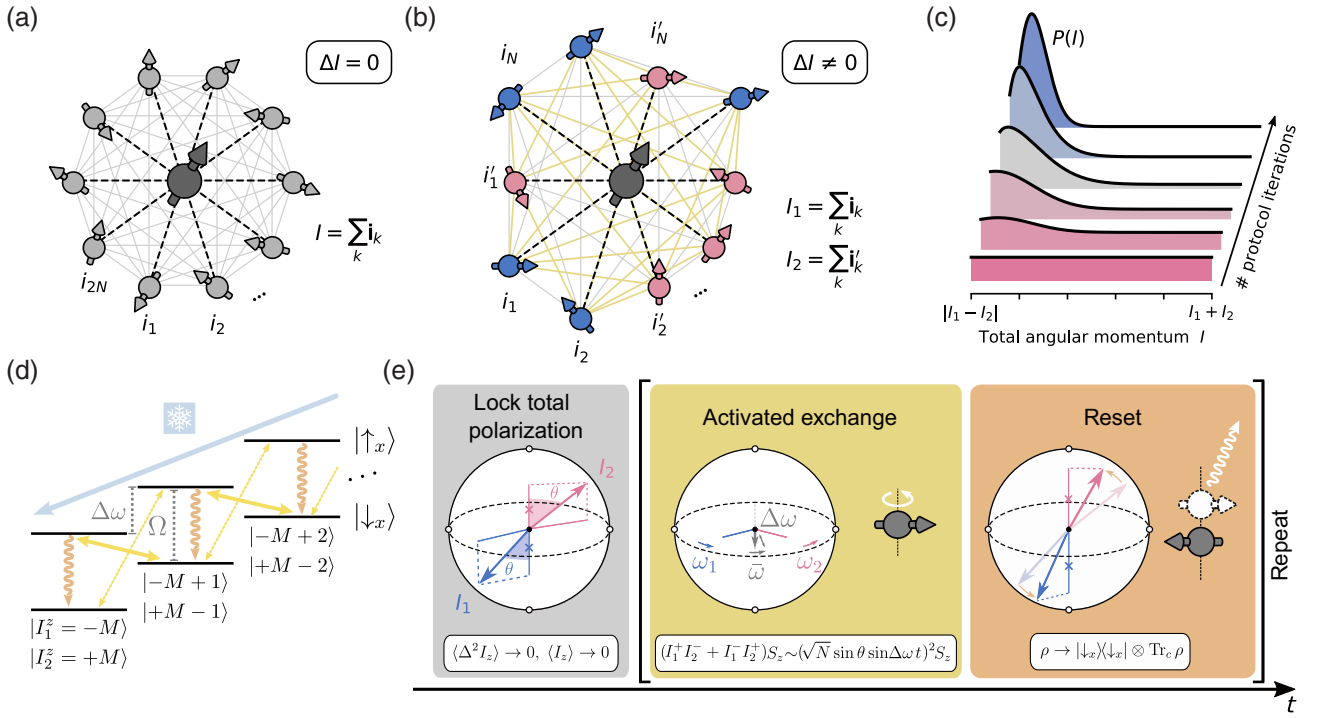

FIG. 1. State engineering in the central-spin system. (a) Perfectly homogeneous central-spin system, symmetry protected from changing its total angular momentum. (b) Symmetry-broken central-spin system, consisting of spin species I_1 and I_2, no longer protected from changing its total angular momentum. (c) Reduction of the total angular momentum magnitude via the state purification protocol, resulting in a narrowed steady-state distribution (blue shaded curve), peaked around $I = N^{-1/4}$. (d) Effective Jaynes-Cummings ladder of states $|I_1^z = -M + n, I_2^z = M - n\rangle$, with anticorrelated I_1^z and I_2^z, where $M = \min(I_1, I_2)$. The thick and faint yellow arrows illustrate the dominant and $2\Delta\omega$-detuned three-body interactions, respectively. The curvy orange arrows represent the central-spin resets. The pale blue arrow displays a net direction of the phase space flow within this effective sideband-cooling process. (e) Stages of antipolarized state preparation. The red and blue arrows within the generalized Bloch spheres denote the total angular momenta of the two species, $\mathbf{I}_1$ and $\mathbf{I}_2$. Stage one (left panel): locking of the total polarization, $I^z = I_1^z + I_2^z$, to zero. Stage two: activation of the three-body interaction (middle panel), equivalent to the back-action sensing, followed by central-spin reset (right panel).

underlying symmetries—see Appendix A). In the discussions to follow, we assign them the value $\sqrt{N/2}$, which is the most likely value for a fully mixed initial state. Our results concerning the first two stages of the protocol hold for all (I_1, I_2) values in an approximate $\sqrt{N/2}$ vicinity (Appendix A), thus capturing all experimentally relevant dynamics. We also note that this easily extends to more than two species.

This situation of two distinguishable spin species makes it possible to alter the magnitude of the total angular momentum, $I = |\mathbf{I}_1 + \mathbf{I}_2|$, and therefore to significantly reduce it [see Fig. 1(c)]. When controlled via a directional pumping process (i.e., cooling), the spin ensembles can be initialized into a pure collective antipolarized state [42]:

$$\left|I_1^z = -M, I_2^z = M\right\rangle \tag{2}$$

with $M = \min(I_1, I_2)$. Such a state contains no coherence between the species, and represents a classical limit to the total angular momentum reduction, featuring noise of $\langle \mathbf{I}^2 \rangle_{\mathrm{cl}} = (I_1 + I_2)(|I_1 - I_2| + 1) \sim \sqrt{N}$; a factor $\sqrt{N}$ lower than that of a thermal state.

Creating entanglement via a controlled phase between the two species can lower the magnitude of the total angular momentum further down to $I = |I_1 - I_2|$. In particular, for $I_1 = I_2$ (a condition that can be enforced via direct measurement of I_1 and I_2; see Appendix A), the quantum limit is reached after the preparation of a many-body singlet, i.e.,

$$|I = 0\rangle = \sum_{n=0}^{2M} \frac{(-1)^n}{\sqrt{2M+1}} \left|I_1^z = -M + n, I_2^z = M - n\right\rangle, \tag{3}$$

expressed uniquely in the $\left|I_1^z = -M + n, I_2^z = M - n\right\rangle$ basis using Clebsh-Gordan coefficients. The many-body singlet is also characterized by a full noise suppression: $\langle \mathbf{I}^2 \rangle_{\mathrm{qu}} = 0$.

B. System Hamiltonian: control via the central spin

We take the general Hamiltonian for a dense central-spin system in an external magnetic field [14], and split the spin ensemble into two spin species $i = 1, 2$:

$$H = \omega_c S_z + \sum_{i=1,2} \omega_i I_i^z + \sum_{i=1,2} a_i \mathbf{S} \cdot \mathbf{I}_i. \tag{4}$$

We consider the regime of high magnetic fields, as defined by a dominant Zeeman interaction $\propto \omega_c$ of the central spin, $\mathbf{S}$. The second term captures the internal energy structure ω_i of the spin ensembles. The last term represents a Heisenberg-type hyperfine coupling ($\propto a_i < \omega_i$) between the central spin and the bath spins. We consider a symmetry breaking between the two spin ensembles $\omega_1 \neq \omega_2$, which in real systems can take myriad forms. Without loss of generality, we assume that $a_1 = a_2 \equiv a$ (cf. Appendix B 2) and $\omega_1 > \omega_2$. In this high-field regime, the central-spin quantization axis is pinned to the z direction, and the hyperfine interaction reduces to [43,44]

$$\begin{aligned} a \sum_{i=1,2} \mathbf{S} \cdot \mathbf{I}_i = {} & a S_z (I_1^z + I_2^z) - \frac{a^2}{4\omega_c} (I_1^z + I_2^z) \\ & + \sum_{i=1,2} \frac{a^2}{4\omega_c} S_z (I_i^+ I_i^- + I_i^- I_i^+) \\ & + \frac{a^2}{2\omega_c} S_z (I_1^+ I_2^- + I_1^- I_2^+) \\ & + \mathcal{O}[(a/\omega_c)^2]. \end{aligned} \tag{5}$$

The leading and only first-order hyperfine term is the collinear interaction (used in total polarization locking). The second term renormalizes the nuclear Zeeman interaction of the ensemble by a negligible amount of $-a^2/4\omega_c \ll \omega_i$. The third and fourth terms contain the effective two-body and three-body interactions, respectively. The former will remain off-resonance during our protocol, while the latter will be critical in cooling and correlating the two spin ensembles.

Exclusively to stabilize the ensemble polarization [22] (that is, to drive dynamic nuclear polarization conditional on the sign of I^z), we also consider that, apart from the Zeeman interaction ($\propto \omega_i$), the ensemble spins are subject to a small eigenstate-mixing interaction ($\propto \nu_i \lesssim \omega_i$) [36], which results in an effective noncollinear term:

$$H_{\mathrm{nc}} = \sum_{i=1,2} \frac{a\nu_i}{2\omega_i} S_z I_i^x + \mathcal{O}[(\nu_i/\omega_i)^2]. \tag{6}$$

Finally, we consider a control of the entire system exclusively via the central spin, represented by a resonant drive of the central spin with strength $\Omega \ll \omega_c$, and work in a rotating frame of reference, under the rotating-wave approximation (Appendix B).

C. Preparation of a pure antipolarized state

Prior to the protocol execution, the spin ensemble is found in a fully mixed state characterized by a density matrix $\rho \propto \mathbb{1}$. The first two stages of our protocol initialize the ensemble to a pure collective state—an antipolarized state of the two spin species [Eq. (2)]—that enables the generation of a many-body singlet of the whole ensemble in the third stage (last section of this article).

Stage 1: polarization locking.—The initial state exhibits maximal uncertainty of the total polarization of the bath $\langle \Delta^2 I^z \rangle \sim \sqrt{N}$, where $I^z = I_1^z + I_2^z$. The first stage of the protocol reduces this uncertainty close to zero using a technique developed in Ref. [16] with InGaAs quantum dots (QDs; where it yielded a state with a polarization fluctuation of ± 2.85 units). In brief terms, the collinear hyperfine interaction [the first term in Eq. (5)] allows the central spin to sense the polarization deviation from the $I^z = 0$ lock point, which induces a Larmor precession around the z axis. Subsequently, this deviation is corrected by a resonantly activated ($\Omega = \omega_1$ or $\Omega = \omega_2$; cf. Ref. [45]) noncollinear interaction [using Eq. (6)] that translates the acquired phase into a change in the total ensemble polarization. Finally, the state of the central spin is reset and this stage is repeated until the ensemble reaches the limit of $\langle I^z \rangle = 0$ and $\langle \Delta^2 I^z \rangle = 0$. An imperfect preparation ($\langle \Delta^2 I^z \rangle \neq 0$) at this stage does not affect the operation of stage 2, which acts on the orthogonal space $I_1^z - I_2^z$; it would, however, affect entanglement generation in stage 3 on par with an uncertainty in the value of M, which we address in Appendix A.

Stage 2: full purification.—From this point on, the noncollinear interaction [Eq. (6)] remains off-resonant. At the end of the first stage, the ensemble's locked zero-polarization state is a mixture of states $\left|I_1^z = -M + n, I_2^z = M - n\right\rangle$, where $n = 0, 1, \ldots, 2M$, for which the remaining uncertainty lies in the polarization of individual species, I_1^z and I_2^z. The second stage of the protocol removes this uncertainty to produce a pure collective state. Doing so relies on the driven activation of the three-body interaction [fourth term of Eq. (5)] achieved by setting $\Omega = \Delta\omega \equiv \omega_1 - \omega_2$. For the central spin initialized in state $|{\downarrow_x}\rangle$, i.e., one of the two eigenstates of the S_x operator ($|{\downarrow_x}\rangle$ and $|{\uparrow_x}\rangle$), this drives the following pair of transitions:

$$\begin{aligned} \left|I_1^z, I_2^z\right\rangle |{\downarrow_x}\rangle &\leftrightarrow \left|I_1^z - 1, I_2^z + 1\right\rangle |{\uparrow_x}\rangle, \\ \left|I_1^z, I_2^z\right\rangle |{\downarrow_x}\rangle &\leftrightarrow \left|I_1^z + 1, I_2^z - 1\right\rangle |{\uparrow_x}\rangle, \end{aligned} \tag{7}$$

with the first on three-body resonance and the second detuned by $2\Delta\omega$ from this resonance (cf. Appendix E).

This can be visualized in an effective Jaynes-Cummings ladder of states [Fig. 1(d)] parameterized by the principal quantum number n corresponding to the $\left|I_1^z = -M + n, I_2^z = M - n\right\rangle$ state. The first (second) line

of Eq. (7) is represented by a single quantum $n \leftrightarrow n-1$ ($n \leftrightarrow n+1$) transition down (up) the ladder. Combined with a central-spin reset $|\uparrow_x\rangle \rightarrow |\downarrow_x\rangle$ applied every half period of the three-body interaction, repeating the activation and reset forms a directional pumping process—equivalent to sideband cooling in harmonic systems [46]—towards the ladder's ground state $n = 0$ (a repeated reset to $|\uparrow_x\rangle$ instead would reverse the direction of the flow). This ground state consists of the fully antipolarized state $\left|I_1^z = -M, I_2^z = M\right\rangle$, which is a pure collective state of the ensemble.

Maintaining the directionality of the pumping process relies on the detuning of $2\Delta\omega$ between the selected transition $\left|I_1^z, I_2^z\right\rangle|\downarrow_x\rangle \leftrightarrow \left|I_1^z - 1, I_2^z + 1\right\rangle|\uparrow_x\rangle$ and the unwanted transition $\left|I_1^z, I_2^z\right\rangle|\downarrow_x\rangle \leftrightarrow \left|I_1^z + 1, I_2^z - 1\right\rangle|\uparrow_x\rangle$ [thick and faint yellow arrows in Fig. 1(d), respectively], which drive the system towards the opposite ends of the ladder. This is sustained as long as the three-body interaction strength, $Na^2/2\omega_c$, remains smaller than $\Delta\omega$. We characterize the directionality with their ratio, which ultimately sets the purification limit:

$$\kappa = \omega_c \Delta\omega/(Na^2). \tag{8}$$

We summarize this two-stage cooling process in Fig. 1(e), where the initial locked state has two spin ensembles with arbitrary but opposite orientations. The second stage relies on locking the central spin into the Larmor precession beat note between two nuclear spin species, allowing polarization exchange between the spin and the ensembles. The timing of the central-spin reset favors a maximum amount of polarization exchange to the central spin. With every reset, the two ensembles become preferentially aligned in a specific orientation.

D. Ideal system dynamics

We verify the convergence of the second stage of the protocol towards the ground state by calculating the full quantum evolution of the system numerically. We treat the ideal case, for which the three-body interaction is fully coherent and the central-spin reset is instantaneous. We repeat this second stage as many times as necessary to reach steady state. For convergence towards the steady state under reasonable computational resources, we choose to work with $N = 32$ bath spins and focus on the $I_1 = I_2 = \sqrt{32/2}$ manifold (see Appendices A and B). We take the first stage of the protocol to be fully capable of confining the ensemble's dynamics to the $I^z = 0$ subspace [16], spanned by $\{\left|I_1^z = -M + n, I_2^z = M - n\right\rangle, n = 0, 1, 2, \ldots, 2M\}$, to which we accordingly restrict our simulation. At the beginning of the simulation, we set the ensemble's density operator, ρ, to an equal statistical mixture of the subspace basis states.

Figure 2(a) shows the central spin's evolution under the activated three-body interaction and confirms the coherent oscillation in the $\{|\downarrow_x\rangle, |\uparrow_x\rangle\}$ basis, with a half period of $\tau_0 \sim 2\pi\omega_c/[a^2(I_1 \times I_2)]$—inversely proportional to the fastest three-body interaction rate (Appendix C). The state of the central spin is instantaneously reset every τ_0, and during the consecutive iterations the magnitude of the acquired $|\uparrow_x\rangle$ population drops to zero as the ensemble approaches its ground state. Semiclassically, this corresponds to a drop in the magnitude of the noise $\langle \mathbf{I}^2 \rangle$ sensed by the central spin [Fig. 2(a)]. We verify this independently, as shown in Fig. 2(b), where $\langle \mathbf{I}^2 \rangle$ saturates to its classical approximate $\sqrt{N}$ limit as the steady state is reached. Figure 2(c) shows the polarizations of each of the two species, I_1^z and I_2^z, as a function of the iteration time. We see that they saturate to maximal and opposite values $I_1^z = +\min(I_1, I_2)$ and $I_2^z = -\min(I_1, I_2)$. Importantly,

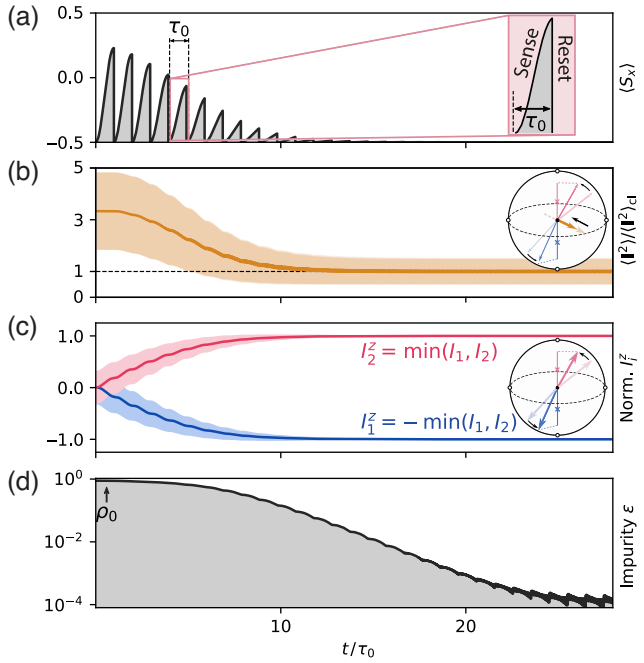

FIG. 2. Ideal system's dynamics for $N = 32$ and $I_1 = I_2 = \sqrt{32/2}$. (a) The expectation value of S_x as a function of the protocol time. Inset: $\langle S_x \rangle$ during a single iteration of sensing and instantaneous reset [cf. the middle and rightmost panels of Fig. 1(e)]. (b) Magnitude (solid orange line) and the uncertainty (shaded area) of $\langle \mathbf{I}^2 \rangle$ as a function of the protocol time, normalized by $\langle \mathbf{I}^2 \rangle_{cl} = (I_1 + I_2)(|I_1 - I_2| + 1)$. Inset: suppression of total I (orange arrow) down to the classical limit. (c) The normalized expectation values of I_1^z and I_2^z (solid blue and red lines, respectively) and their uncertainties (corresponding shaded areas) as a function of the protocol time. The normalization involves dividing the y-axis values by $\min(I_1, I_2)$. Inset: $\mathbf{I}_1$ and $\mathbf{I}_2$ dynamics towards a pure antipolarized state. (d) The ensemble impurity ϵ as a function of the protocol time. Here ρ_0 denotes the state of the bath at the beginning of the second stage of the protocol. The x axis is shared across the panels.

at the longest iteration times, their uncertainties approach zero, as expected for a pure antipolarized state.

We quantify the quality of state preparation following our protocol using the bath state impurity

$$\epsilon = 1 - \mathrm{Tr}\rho^2, \tag{9}$$

where ρ is the density operator of the bath. For a pure state, this measure is known to reach zero. In our simulation, we selected a directionality parameter of $\kappa = 5$ [Eq. (8)] as an example case. Figure 2(d) shows that, for this value of κ, the impurity reaches a steady-state value of $\epsilon \approx 10^{-4}$, which represents a negligible initialization error. After settling, the system is trapped in an oscillatory limit cycle, resulting from the competition of $|\downarrow_x\rangle \left|I_1^z, I_2^z\right\rangle \leftrightarrow |\uparrow_x\rangle \left|I_1^z - 1, I_2^z + 1\right\rangle$ and $|\downarrow_x\rangle \left|I_1^z, I_2^z\right\rangle \leftrightarrow |\uparrow_x\rangle \left|I_1^z + 1, I_2^z - 1\right\rangle$ transitions. The impurity ϵ can be made arbitrarily small by increasing κ (e.g., by increasing ω_c via an external magnetic field), which we address in the following section.

E. Dependence of protocol performance on system parameters

In the absence of dephasing and spin diffusion, there remains a fundamental trade-off between impurity ϵ and the convergence time to steady state T_c. This is because reducing the three-body interaction—increasing κ—ensures a smaller contribution from off-resonant processes, thus reducing the initialization error while slowing the dynamics towards the steady state. For $\kappa \to \infty$, one could expect bringing the impurity ϵ arbitrarily close to zero at the cost of a prohibitively long convergence time, T_c.

To visualize the achievable steady-state impurities and related convergence times, we run a complete simulation of our pulsed protocol for a range of values of κ and for $N = 8$, as well as $N = 128$. Figure 3(a) confirms the clear trend of purity improvement with an increase in κ, where substantial degrees of purification are achieved past $\kappa \gtrsim 1$. Figure 3(b) shows the inverse N dependence of the half period of the collective three-body exchange, $\tau_0 \sim 4\pi\omega_c/Na^2$, and the number of stage iterations required to reach convergence proportional to N. The convergence time is a simple product of these two quantities and thus combines to

$$T_c \sim 16\pi\omega_c/a^2, \tag{10}$$

indicating that the convergence time is dependent purely on the three-body interaction strength, and not the system size. The interaction strength may however still depend on N, as is the case in physical platforms where said interaction results from the spatial overlap of the central-spin wave function with that of the ensemble; there, $a = A/N$ with A characterizing the total interaction strength (see Appendix D).

Verifying the above trends in the large-N limit becomes computationally prohibitive. As an efficient way to extend our results into this regime, we turn to a steady-state solver of a quantum master equation in which the coherent three-body exchange proceeds continuously and simultaneously with a central spin reset whose rate is $\Gamma_{\mathrm{op}} = 2\pi/\tau_0$. Figure 3(c) displays the steady-state impurity, ϵ, for N up to 10 000 and for the same range of values of κ as in Fig. 3(a). This confirms effective purification for $\kappa \gtrsim 1$ for large N. The solid black curve in Fig. 3(c) is the prediction from a simple rate equation (Appendix C), i.e., $N \to \infty$, which overlaps with the steady-state model in the large-N limit. Both models feature a $\epsilon \sim \kappa^{-2}$ roll-off, as obtained analytically from a first-order expansion of the impurity in the rate equation model (see Appendix C). As shown in Fig. 3(d), eigenvalue analysis of the rate equation allows us to calculate the convergence time, T_c, agreeing with the size-independent $T_c \sim 16\pi\omega_c/a^2$ behavior observed in the pulsed model [Fig. 3(b)].

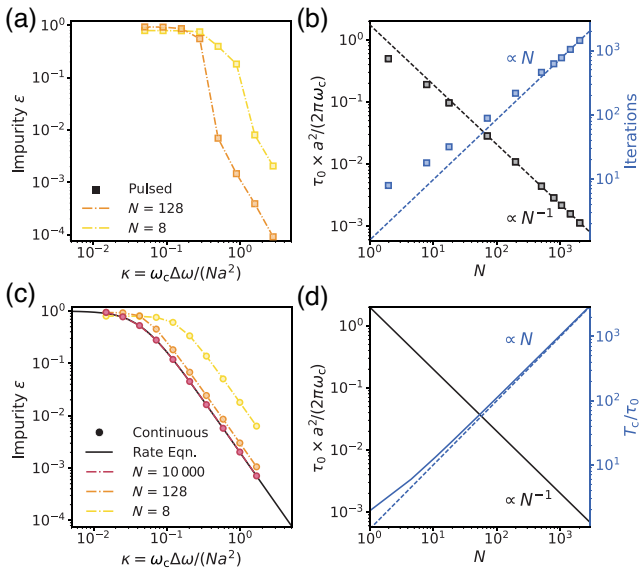

FIG. 3. Dependence on system parameters. (a) Steady-state impurity, ϵ, as a function of the directionality parameter, $\kappa = \omega_c\Delta\omega/(Na^2)$. (b) Normalized three-body interaction half periods (i.e., the pulse durations), τ_0 (black squares), and the numbers of stage iterations (blue squares) required to reach convergence in the pulsed protocol, as a function of N. The number of iterations was calculated as 3 times the $1/e$-drop time in the impurity's exponent to the settled value. The dashed lines illustrate the asymptotic behavior, $N \to \infty$, of both quantities. (c) The κ dependence of impurity, ϵ, in the continuous protocol. The solid black line displays a corresponding solution from the rate equation model, which correctly captures the high-N limit. (d) Prediction of the convergence results in Fig. 3(b) using the rate equation model.

Comparing the pulsed [Fig. 3(a)] and continuous [Fig. 3(c)] protocol performance, we note that maintaining the temporal separation between the central-spin reset and activation of the three-body interaction with the ensemble allows reaching lower steady-state impurities. This property, illustrated by comparing experiments done in the continuous [22] and pulsed [16] regimes, can be straightforwardly explained: continuously measuring the central spin reduces its ability to sense the ensemble noise and, in turn, limits the achievable purity.

F. Resilience to system imperfections

Real physical systems deviate from the idealized behavior considered so far, as they are affected by various forms of dephasing and spin diffusion, through which they recover thermal equilibrium. For instance, ensemble inhomogeneous dephasing can occur if the ensemble spins have a spread of Larmor precession frequencies $\sqrt{\Delta^2\omega_i} > 0$ [16,17], or during the central spin resets if the reset time τ_r is a significant fraction of the activation time τ_0 (cf. Appendix D). Meanwhile, spin diffusion may result from interactions of the ensemble with environments that are not directly coupled to the central spin [35,47,48]. Moreover, since each stage of our purification protocol relies on the exchange dynamics between the central spin and the ensemble, the protocol is as sensitive to the central-spin dephasing as it is to that of the ensemble (Appendix B). In our model, these dephasing processes are characterized together by their total rate Γ_{deph}. Similarly, we factor in the spin diffusion, proceeding at rate Γ_{diff} independent of the macrostate. This phenomenological approach provides an accurate proxy for the varied system-specific imperfections (e.g., individual nuclear spin dephasing) while maintaining computational tractability thanks to imposed conservation of $\mathbf{I}_1$ and $\mathbf{I}_2$. In a regime where the dephasing dynamics break this conservation on timescales shorter than the convergence time, T_c, this would prevent the complete saturation ($\langle n\rangle = 0$) of states with fixed $M \sim \sqrt{N/2}$. Interestingly, this situation does not compromise the conceptual viability of the proposal: the net flow towards $\langle n\rangle = 0$ (independent of M) will force now directable $\mathbf{I}_1$ and $\mathbf{I}_2$ to larger values $M \gg \sqrt{N/2}$ [49] for which the nuclear state retains its desirable properties (see Appendix A).

Ahead of the calculation, we anticipate two diffusion-mitigating strategies possible with simple protocol adjustments that do not require additional experimental controls. Firstly, we observe that diffusion can lead to population leakage outside of the considered $I^z = 0$ ladder of states. This can be prevented by alternating between the two first stages of the protocol on short timescales to maintain a population flow towards $I^z = 0$ and to maximize $|I_1^z - I_2^z|$. Secondly, due to variation of the collective enhancement factor along the ladder (Appendix C), chirping the activation time from τ_0 up to about $\tau_0\sqrt{N/8}$ (the slowest three-body interaction timescale) can help in optimizing the population flow rate against the state-independent spin diffusion (Appendix B 4).

Using the rate equation approach (Appendix C), and considering the scenario representative of the τ chirp (i.e., setting $\tau = \tau_0\sqrt{N/8}$), we calculate the steady-state impurity, ϵ, as a function of the normalized dephasing and diffusion rates, $\Gamma_{\text{deph}}\tau_0\sqrt{N}/(2\pi)$ and $\Gamma_{\text{diff}}\tau_0\sqrt{N}/(2\pi)$, respectively. Figure 4(a) identifies two regimes of protocol performance in which distinct physical mechanisms dictate the fundamental limit on achievable impurity

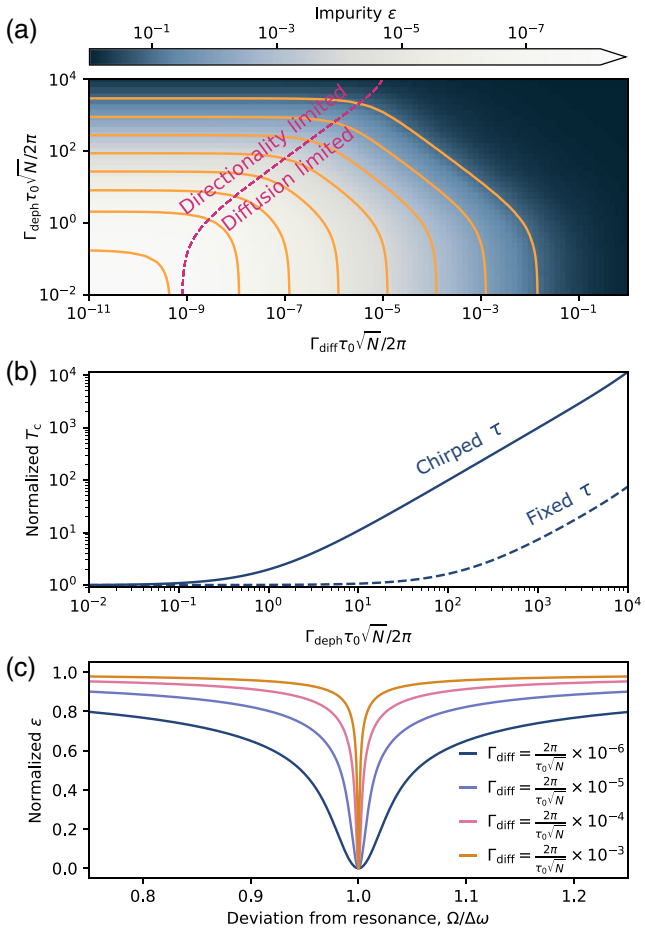

FIG. 4. Resilience to dephasing and spin diffusion. (a) Impurity as a function of the normalized spin diffusion rate, $\Gamma_{\text{diff}}\tau_0\sqrt{N}/(2\pi)$, and the normalized total dephasing rate, $\Gamma_{\text{deph}}\tau_0\sqrt{N}/(2\pi)$, calculated at the $\Omega = \Delta\omega$ resonance for $N = 10^5$. The orange solid lines are contours of $\epsilon = 10^{-m}$ for $m = 1, 2, \ldots, 8$. The pink dashed line is a boundary between the directionality-limited regime and the diffusion-limited regime. (b) Normalized convergence time as a function of the normalized total dephasing rate for protocols with fixed activation time ($\tau = \tau_0$) and chirped activation time (up to $\tau = \tau_0\sqrt{N/8}$). (c) Normalized impurity as a function of deviation from the $\Omega = \Delta\omega$ resonance for increasing levels of spin diffusion.

(Appendix C). To the left of the pink dashed curve in Fig. 4(a), the impurity is limited by directionality—that is, κ—as reflected by the expression

$$\epsilon \approx \frac{2}{1+32N\kappa^2/\mathcal{D}_{\rm dir}}, \tag{11}$$

where

$$\mathcal{D}_{\rm dir} = \left(1+\frac{\Gamma_{\rm deph}\tau_0\sqrt{N}}{2\pi}\right)\left(1+2\frac{\Gamma_{\rm deph}\tau_0\sqrt{N}}{2\pi}\right). \tag{12}$$

In the second regime, on the right of the pink curve in Fig. 4(a), the impurity is governed by spin diffusion, as captured by

$$\epsilon \approx \frac{8\mathcal{D}_{\rm diff}}{4\mathcal{D}_{\rm diff}+1}, \tag{13}$$

where

$$\mathcal{D}_{\rm diff} = \left(1+\frac{\Gamma_{\rm deph}\tau_0\sqrt{N}}{2\pi}\right)\frac{\Gamma_{\rm diff}\tau_0\sqrt{N}}{2\pi}. \tag{14}$$

It is clear that even low relative rates of spin diffusion can be detrimental to the achievable impurity. Moreover, dephasing and spin diffusion alter two other performance measures: dephasing prolongs the convergence time, while diffusion reduces tolerance to detuning from the $\Omega = \Delta\omega$ resonance. Figure 4(b) displays a dependence of convergence time, T_c, on the normalized dephasing rate for the protocols with the activation time fixed to τ_0 (the dashed curve), and chirped up to $\tau_0\sqrt{N/8}$ (the solid line). The curves evidence that dephasing has a significant effect only when its timescale becomes comparable to the activation time, that is, $\Gamma_{\rm deph}\tau/2\pi \sim 1$. For the general protocol with activation time chirped up to τ, the convergence time is well approximated by

$$T_c \approx 4N\tau\left(1+\frac{\Gamma_{\rm deph}\tau}{2\pi}\right). \tag{15}$$

Figure 4(c) shows the normalized impurity as a function of deviation from the $\Omega = \Delta\omega$ resonance for increasing levels of spin diffusion. As expected, when diffusion becomes faster, the resonance condition becomes more strict, as the protocol loses tolerance to imperfections that decreases the rate of population flow down the ladder.

We note that impurity is a particularly punishing measure for large spin ensembles, and even significant rates of spin diffusion do not preclude a build-up of nearly complete antipolarization, reflected by a steady-state principal quantum number $\langle n\rangle \approx 0$, as we show in the next section.

G. Benchmarking candidate material platforms

Throughout this work, we have identified the three platform-agnostic control parameters determining the protocol performance: the directionality parameter, κ, the normalized total dephasing rate, $\Gamma_{\rm deph}\tau_0\sqrt{N}/(2\pi)$, and the normalized spin diffusion rate, $\Gamma_{\rm diff}\tau_0\sqrt{N}/(2\pi)$. We now evaluate these parameters for candidate physical systems and quantify the corresponding bounds on steady-state ensemble impurities, ϵ, average principal quantum numbers, $\langle n\rangle$, as well as the protocol convergence times, T_c, as shown in Fig. 5.

We restrict our analysis to the physical platforms that naturally realize dense central-spin systems [see the Hamiltonian of Eq. (4)], and in which the rudimentary protocol ingredients, like the control and reset of the central-spin state, have been demonstrated previously. Our nonexhaustive selection of the candidate systems includes gate-defined QDs, lattice-matched GaAs-AlGaAs QDs, Stranski-Krastanov InGaAs QDs, and rare-earth ions (REIs). The system-specific parameters used in the calculations are summarised in Appendix D (see Tables I–IV).

For QD systems, the two spin species that break ensemble symmetry are simply two nuclear-spin species with different gyromagnetic ratios: gallium and arsenic. Of all considered platforms in this family, the GaAs QDs feature the fastest three-body interaction dynamics, with $\tau_0/B \sim 2.2\,\mu$s/T. In comparison, in InGaAs QDs $\tau_0/B \sim 9.9\,\mu$s/T and in gate-defined QDs $\tau_0/B \sim 132.2\,\mu$s/T, the latter featuring the slowest dynamics due to a system size that is typically an order of magnitude larger, as reflected in a correspondingly reduced single nucleus hyperfine constant (Appendix D).

In all three cases, the total dephasing is dominated by the inhomogeneity of nuclear quadrupolar shifts: in GaAs and gate-defined QDs $\Gamma_{\rm deph} \sim 2\pi \times 10$ kHz [15,25], while in InGaAs QDs $\Gamma_{\rm deph} \sim 2\pi \times 10$ MHz [26]. We observe that $\kappa \gtrsim 1$ for all QD platforms and across the whole considered magnetic field ranges (Appendix D). This would guarantee reaching low impurities, even for the assessed levels of dephasing, if the dynamics belonged to the directionality-limited regime [see Fig. 5(a)].

Under current realizations, these systems belong to the diffusion-limited regime. In gate-defined QDs, spin diffusion proceeding at a rate of $\Gamma_{\rm diff} \sim 2\pi \times 76$ kHz is a major roadblock to a high protocol performance [48]. In this respect, the InGaAs QDs perform best ($\Gamma_{\rm diff} \sim 2\pi \times 15$ Hz), as in their case, the spin diffusion is inhibited by quadrupolar inhomogeneity [50,51]. The spin diffusion rates in GaAs QDs take on an intermediate value ($\Gamma_{\rm diff} \sim 2\pi \times 125$ Hz) [52], as naively expected based on the reduced quadrupolar inhomogeneity relative to InGaAs QDs, yet a better defined QD boundary compared to the gate-defined QDs. As shown in Fig. 5(b), the QD platforms

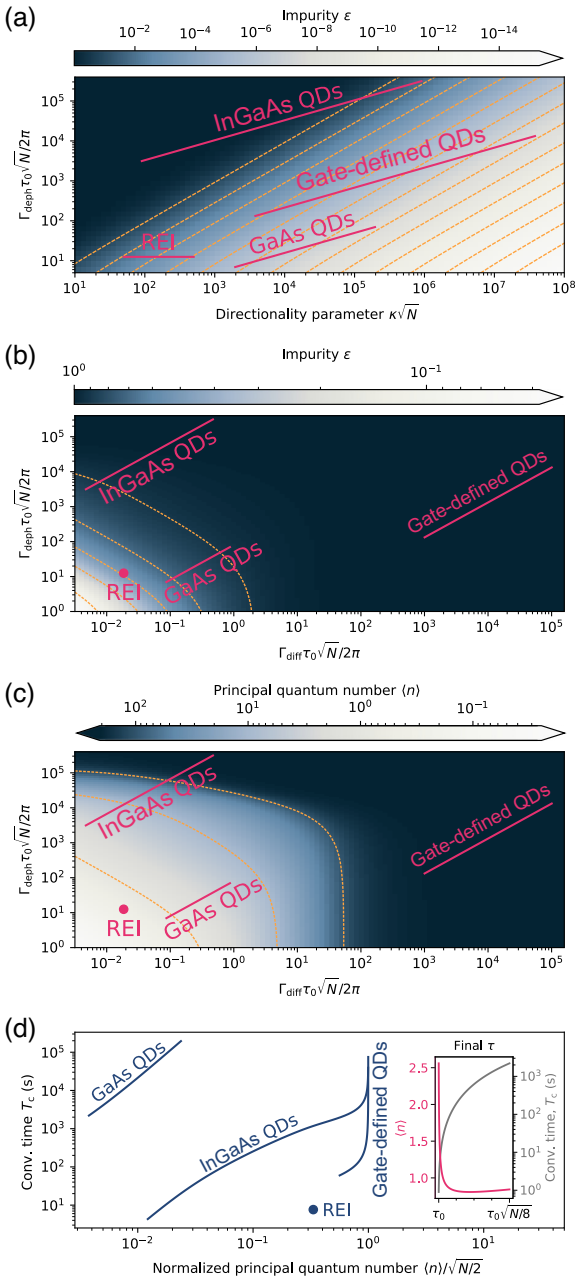

FIG. 5. Benchmarking candidate material platforms. (a) Impurity as a function of the platform-agnostic parameters, $\kappa\sqrt{N}$ and $\Gamma_{\text{deph}}\tau_0\sqrt{N}/2\pi$, calculated assuming that $\Gamma_{\text{diff}}\tau_0\sqrt{N}/2\pi = 0$. Orange dashed contours represent impurities increasing exponentially from 10^{-1} to 10^{-14}. Solid violet lines correspond to the typical operating regimes for selected candidate platforms; the corresponding ranges of κ are used throughout the figure. (b) Impurity calculated for realistic rates of total dephasing, $\Gamma_{\text{deph}}\tau_0\sqrt{N}/2\pi$, and spin diffusion, $\Gamma_{\text{diff}}\tau_0\sqrt{N}/2\pi$. Orange dashed contours represent $\epsilon = 0.1, 0.3, 0.5, 0.7, 0.9$. (c) Corresponding average principal quantum number, $\langle n\rangle$. Orange dashed contours represent $\langle n\rangle = 1, 10, 100$. (d) Summary of the achievable normalized principal quantum numbers and convergence times for the candidate platforms. Inset: the $T_c/\langle n\rangle$ trade-off in GaAs QDs for a range of final activation times, τ, of a chirped protocol.

are expected to exhibit non-negligible ensemble impurities ($\epsilon > 0.5$) following stage 2 of the protocol. Nonetheless, the average principal quantum number, $\langle n\rangle$, achieved in the InGaAs and GaAs QDs [Fig. 5(c)] indicates a substantial degree of antipolarization, which remains a useful starting point for the next stage of the protocol (see the next section). Finally, in typical experiments on gate-defined [15,53] and GaAs QDs [25,54], individual dephasing of the nuclear spins randomizes precession of nuclear polarization within about 100 μs (in the absence of dynamical decoupling), which is significantly shorter than the expected convergence time T_c of stage 2. This would place these systems in a regime where $\mathbf{I}_1$ and $\mathbf{I}_2$ are not conserved and where, as a result of the pumping induced by stage 2, the dynamics will occur at larger effective values of N (see Sec. II F and Appendix A), but where otherwise the nuclear state is expected to retain its desirable properties [23].

We now turn our attention to REI systems—specifically to $^{171}Yb^{3+} : YVO_4$, recently used to demonstrate quantum-state transfer between a ^{171}Yb electronic central spin and the second shell of the nearest ^{51}V nuclei [19]. This system belongs to the regime of small but dense central-spin systems and offers little tunability with an external magnetic field as all nuclear spins are of the same species. However, the nuclear-spin shells surrounding the central spin can be distinguished via quadrupolar shifts, allowing a set of values for the effective $\Delta\omega$ (Appendix D). The required central-spin-mediated three-body interaction arises as a second-order magnetic dipole-dipole coupling between two of the first, second, and higher shells of ^{51}V nuclei interfaced with the ^{171}Yb. The said interaction leads to dynamics on a $\tau_0 \sim 5$-ms timescale. REIs perform best of all considered platforms based on high values of the directionality parameter ($\kappa \sim$ 25–250) and relatively low levels of spin diffusion ($\Gamma_{\text{diff}} \sim 2\pi \times 1.85$ Hz) and dephasing ($\Gamma_{\text{deph}} \sim 2\pi \times 1.25$ kHz); see Figs. 5(a)–5(c).

Figure 5(d) summarizes our platform survey, showing, for each system, the expected convergence times, T_c, as well as the principal quantum numbers, $\langle n\rangle$, normalized by $\sqrt{N/2}$ (that is, the extent of the $I^z = 0$ ladder of states). Because of spin diffusion, the optimal working points for all QD platforms correspond to the lowest magnetic fields that allow for state readout. In InGaAs QDs and gate-defined QDs, the chirped-τ protocols do not improve the performance [their respective curves in Fig. 5(d) correspond to the fixed-τ protocols], whereas in GaAs QDs the chirp helps to achieve $\langle n\rangle < 1$ within a reasonable convergence time of $T_c \sim 200$ s (the corresponding curve corresponds to a chirped-τ protocol). This timescale can be significantly lowered below $T_c \sim 1$ s by lowering the final τ during the chirp close to τ_0. As depicted in the inset of Fig. 5(d), this comes at the cost of a slight rise in $\langle n\rangle$.

H. Preparation of a many-body singlet

The singlet state $|I=0\rangle$ is a superposition of all $\left|I_1^z=-M+n,\, I_2^z=M-n\right\rangle$ eigenstates with a $\propto(-1)^n$ phase on each state, as shown in Eq. (3). Importantly, it can be engineered exactly only if $I_1=I_2=M$.

Having established a pure antipolarized state of the two subensembles (i.e., $n=0$) following the first two stages of the protocol, the third and final stage will prepare the singlet state by weaving an alternating phase into the Jaynes-Cummings ladder, as shown in Fig. 6(a). We stress that the many-body singlet state is *not* an eigenstate of our system Hamiltonian; however, it refocuses every $\Delta t=2\pi/\Delta\omega$ following the protocol termination (Appendix E).

Initially, we consider only the ideal execution of this final stage involving unitary gates, free of any dephasing. This is to confirm that collective effects do not stand in the way of precise quantum-superposition engineering. We work in a frame corotating with $\Omega S_x+\Delta\omega(I_1^z-I_2^z)/2$. For the sake of clarity, we outline the ideal protocol steps assuming that the effective Jaynes-Cummings ladder has $2M+1=2^K$ rungs, corresponding to a total number of ensemble spins $N\sim(2^K-1)^2/2$; the generalization to arbitrary N is straightforward. In the first instance, we take a simplified scenario in which the three-body-interaction is independent of the $\left|I_1^z=-M+n,\, I_2^z=M-n\right\rangle$ state; we later take the dependence on n into account.

We apply the following sequence of unitary operations, starting from state

$$|\psi_0\rangle=|\downarrow_x\rangle\left|I_1^z=-M,\, I_2^z=M\right\rangle. \tag{16}$$

(i) A central spin $(\pi/2)_z$ gate, giving state

$$\frac{1}{\sqrt{2}}(|\downarrow_x\rangle-i\,|\uparrow_x\rangle)\left|I_1^z=-M,\, I_2^z=M\right\rangle, \tag{17}$$

as illustrated in the second level diagram from the left in Fig. 6(a).

(ii) A three-body-interaction π gate, $U(\tau)=U_\pi$, where τ is the interaction time, and which up to a global phase leaves the system in state

$$|\psi_1\rangle=\frac{1}{\sqrt{2}}|\downarrow_x\rangle\left(\left|I_1^z=-M,\, I_2^z=M\right\rangle-\left|I_1^z=-M+1,\, I_2^z=M-1\right\rangle\right), \tag{18}$$

as shown in the third-level diagram from the left in Fig. 6(a).

Together, this pair of gates $(\pi/2)_z$ and U_π inject entanglement into the spin ensemble via the central spin. We combine them into a composite gate S_1, as shown in Fig. 6(a). Application of this gate doubles the overlap with the singlet state, $|\langle\psi_1|(|\downarrow_x\rangle|I=0\rangle)|^2$, from that of the initial state, $|\langle\psi_0|(|\downarrow_x\rangle|I=0\rangle)|^2$. To increase this overlap further, we apply an extended composite gate, S_2, which contains two steps: (i) entanglement injection using S_1 [the fourth- and fifth-level diagrams from the left in Fig. 6(a)] and (ii) phase redistribution onto the $\left|I_1^z=-M+n,\, I_2^z=M-n\right\rangle$ states with $n=0,1,2,3$ using a central-spin $(\pi)_z$ gate and a three-body-interaction π gate [the two rightmost-level diagrams in Fig. 6(a)]. We generalize this sequence to a composite gate S_K, for which the phase redistribution is applied $2^{K-1}-1$ times [gray box in Fig. 6(b)]. Each application of a phase redistribution subsequence brings the next highest rung on the ladder into the ensemble superposition state. As a result, the overlap of system state $\left|\psi_j\right\rangle$ with the many-body singlet state $|\left\langle\psi_j\right|(|\downarrow_x\rangle|I=0\rangle)|^2$ doubles at each step of a sequence of composite gates S_j for $j=1,2,\ldots,K$.

The modular structure of this algorithm is advantageous in terms of minimizing the impact of the central-spin dephasing on the ensemble state preparation. It is sufficient for the central spin to stay coherent over a given S_j gate duration, after which it can be safely reinitialized. This opens up the possibility of built-in error detection following each gate S as any bright electron population would indicate failure of the gate. We note that the phase redistribution is the most operation-costly subsequence, as it involves 2^j-2 gates within each S_j gate. Nevertheless, the protocol complexity remains linear with the number of states along the ladder 2^K as the total number of gates in a complete sequence is $2(2^K-1)$.

We demonstrate the performance of this algorithm in Fig. 6(c), using the trace distance from the engineered state to the singlet state as a function of the total number of gates (gray squares). For $K=4$ ($N=112$), we can visualize the steady progression from $|\psi_0\rangle$ towards the singlet state $|\downarrow_x\rangle|I=0\rangle$ as the algorithm steps through the sequence of composite gates S_1 to S_4, culminating in an exact preparation where the final trace distance reaches zero. The classical limit $\langle\mathbf{I}^2\rangle_{\mathrm{cl}}\sim\sqrt{N}$ is overcome as soon as the sequence begins to inject entanglement into the ensemble, and reaches the quantum limit of $\langle\mathbf{I}^2\rangle_{\mathrm{qu}}=0$ at its termination. Interestingly, this happens at the expense of raising the uncertainty in I_1^z and I_2^z towards their thermal values of about $\sqrt{N}$, akin to squeezing.

We now turn to the more realistic description of the spin ensemble for which the three-body interaction π gate time depends on state $\left|I_1^z=-M+n,\, I_2^z=M-n\right\rangle$. This interaction time will take on values from about $2M$ (for $n=0,2M$) to about $M(M+1)$ (for $n=M$) across the ladder (Appendix E). While this behavior complicates the algorithm implementation, the core structure used to inject entanglement and redistribute phase remains in place. With the right choice of three-body interaction times, τ, and the central-spin z-gate phases, ϕ, it is possible to reach

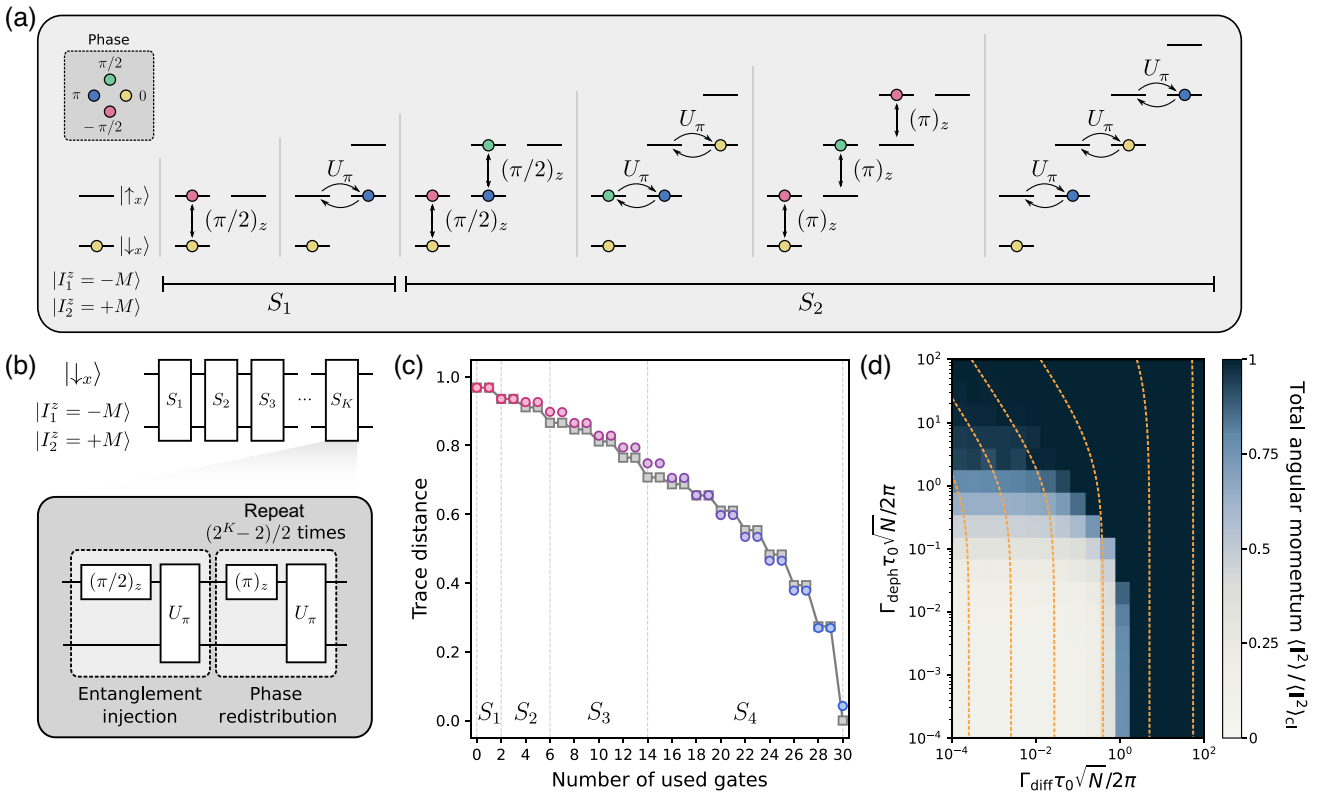

FIG. 6. Reaching a quantum limit. (a) Action of the unitary gates (black arrows) along the effective Jaynes-Cummings ladder of $|I_1^z = -M + n, I_2^z = M - n\rangle$ states, where $M = \min(I_1, I_2)$. The illustrated sequence of six gates prepares a many-body singlet for $K = 2$. The inset displays a relative phase color coding applied throughout the panel. The global phase is factored out, leaving the lowest-energy state with a zero reference phase. (b) Concatenation of the composite S_j gates turns the antipolarized state into a many-body singlet. The gray box contains a quantum circuit corresponding to the S_K gate for an arbitrary integer K. (c) Trace distance from a singlet state as a function of the number of singlet-preparing gates used within the simplified (gray squares) and real (circles) systems with $K = 4$ (i.e., $N = 112$), following the exact and variational-searched protocols, respectively. The red-to-blue gradient indicates that the structure of the optimal protocol (discussed in Appendix E) varies with the number of used gates. (d) Total angular momenta of optimally entangled ensembles (with $K = 3$) in the presence of increasing levels of spin diffusion and dephasing. The orange dashed lines represent contours of $\langle n\rangle = 10^{-3}, 10^{-2}, 10^{-1}, 10^0, 10^1, 10^2$ achieved prior to the final protocol stage, for the corresponding levels of dephasing and spin diffusion.

the singlet state. To do so, we treat the sequence parameters $\{\tau_i, \phi_i\}$ variationally for each gate to minimize the (Hilbert-Schmidt) trace distance to the singlet state from

$$|\psi\rangle = \overleftarrow{\prod_{i=0}} (U(\tau_i) \cdot (\phi_i)_z)\, |\downarrow_x\rangle\, |I_1^z = -M, I_2^z = M\rangle. \quad (19)$$

Formally, this involves an optimization over an approximately 2^K-dimensional space of parameters, for which we employ a gradient-descent algorithm (Appendix E and Ref. [55]). The resulting trace distances for the sequences of increasing length are presented in Fig. 6(c) as the colored circles (red-to-blue gradient is consistent with the color coding used in Appendix E). Strikingly, our algorithm arrives within a trace distance of a few percent from the singlet state.

Next, we assess the effect of dephasing and spin diffusion on this final stage of the protocol. Trace distance from the exact singlet state, much like purity, is a particularly punishing metric in the presence of current levels of imperfections. Nonetheless, we can perform our variational optimization to reach "singletlike states," that is, those that exhibit a largely reduced total angular momentum $\langle \mathbf{I}^2\rangle$ relative to the classical limit. We use $\langle \mathbf{I}^2\rangle$ directly as a cost function and recover the optimal total angular momentum reduction when $\Gamma_{\text{diff}}\tau_0\sqrt{N}/2\pi$ and $\Gamma_{\text{deph}}\tau_0\sqrt{N}/2\pi$ are both $\ll 1$ [see Fig. 6(d)]. Unsurprisingly, this stage of the protocol is far more sensitive to dephasing than the first and second stages. Still, our optimization procedure allows us to design sequences that reduce $\langle \mathbf{I}^2\rangle$ even in the $\Gamma_{\text{diff}}\tau_0\sqrt{N}/2\pi \sim 1$ and $\Gamma_{\text{deph}}\tau_0\sqrt{N}/2\pi \sim 1$ cases. We overlay the results of Fig. 5(c) on achievable $\langle n\rangle$ following stage 2, which confirms that current experimental

platforms could be used to measure singletlike states in a proof-of-concept experiment.

Finally, we highlight that the prospects of near-term implementations of our protocol in platforms with $N \sim 10^5$ hinge on achieving low gate errors—on par with those achieved in atomic systems [56]. In the aforementioned QD systems, the last and longest composite gate, S_9, requires 510 three-body electron-nuclear gates between electron resets. Experimentally, single-qubit gates currently feature an approximate 0.007 error [25], as a lower bound on the three-body gate error. We thus estimate that a reduction in gate error by a factor of 10–100 would be sufficient for a full protocol implementation. The other experimental overhead in our protocol—the necessity for postselection based on the measurement of I_1 and I_2 (see Appendix A)—is greatly facilitated by recent results on photon collection in QD systems exceeding 50% end-to-end efficiency [57,58].

Interestingly, by applying our variational approach to reduce the total angular momentum of the ensemble (Appendix E 3 d), we confirmed that robust quantum-state preparation can occur free of the $I_1 = I_2 = M$ constraint and thus without postselection. This occurred with a significantly reduced number of gates over which the convergence was achieved and renders the proposed singletlike state preparation compatible with available gate fidelities and experimental state of the art.

III. CONCLUSIONS AND OUTLOOKS

In this work, we have proposed a protocol that can initialize a spin ensemble into a pure antipolarized state and steer it towards a many-body entangled singlet state—exclusively by using a single central-spin qubit. To do so, we have made use of the three-body interaction naturally present in dense spin ensembles and shown that it can be harnessed by breaking the ensemble into two spin species. We note that such breaking of ensemble symmetry can take multiple forms, including, but not limited to, nuclear-spin species with different gyromagnetic ratios [26] or high-spin species that split into two effective qubit ensembles under the influence of electric field gradients (e.g., from strain) [54].

We have suggested several platforms where our algorithm would be realizable, and where a nearly complete degree of antipolarization ($\langle n \rangle \approx 0$) can be achieved even in the presence of typical levels of dephasing and spin diffusion. A reduction of the total angular momentum well below the classical limit—i.e., a singletlike state—is possible under these conditions. While a true many-body singlet engineered out of a unity purity state is currently out of reach for our suggested platforms, vast improvements are possible [25] to further reduce spin diffusion and dephasing rates through materials engineering [51] and direct decoupling techniques [19,54]. Extensions of our scheme to include single-shot readout of the electron spin, as demonstrated in all suggested platforms [59–61], would make it possible to herald the initialized nuclear state required for the generation of a many-body singlet.

From the perspective of an electron spin qubit hosted in a material with nonzero nuclear spins, a singlet state of its surrounding spin ensemble (or any state that approaches singletlike properties) would dramatically boost its coherence—both homogeneous and inhomogeneous noise sources [26] would be quenched. From the perspective of leveraging this spin ensemble as a quantum memory resource [39], initialization to a pure collective state at the end of stage 2 already realizes a step necessary to run an algorithm with unit fidelity [62], and the availability of two antipolarized species could even be extended to a two-mode register. The state-engineering recipes that we have established could be extended to more elaborate computational [63] and error-correcting [21] algorithms. Fundamentally, tracking a many-body state in the presence of tuneable interactions can reveal the entanglement dynamics in and out of the central-spin system, opening an experimental window onto quantum information scrambling and area laws for entanglement entropy.

ACKNOWLEDGMENTS

We acknowledge support from the US Office of Naval Research Global (N62909-19-1-2115). D.A.G. acknowledges a Royal Society University Research Fellowship, and C.LG. a Dorothy Hodgkin Royal Society Fellowship. L.Z. acknowledges support from the EPSRC DTP. We also thank S. Economou and E. Barnes for fruitful discussions.

APPENDIX A: MANIFOLD DEGENERACIES

Within the manuscript we make a statement about the dynamics in the $I_1 = I_2 = \sqrt{N/2}$ manifold being representative of the complete ensemble dynamics. This follows from the (I_1, I_2)-manifold degeneracy, captured by the

$$p(I_1, I_2) \propto I_1(I_1+1)\, I_2(I_2+1)\, e^{-2(I_1^2+I_2^2)/N} \tag{A1}$$

probability distribution for an ensemble initially at infinite temperature [16]. As shown in Fig. 7, this distribution features a peak at $\sqrt{N/2}$ of width $\propto \sqrt{N/2}$, and an exponentially suppressed high-I_i tail. Therefore, when randomly sampling the (I_1, I_2) distribution in the experiment, a majority of the experimental runs will satisfy $I_1, I_2 \sim \sqrt{N/2}$.

1. Implications for the protocol

A typical deviation from $I_1 = I_2 = \sqrt{N/2}$ features $I_1 \neq I_2$. In Appendix B 1, we study the protocol performance in the $I_1 \neq I_2$ case, and compare it to the $I_1 = I_2$ case (studied in the main text) to find the same degree of

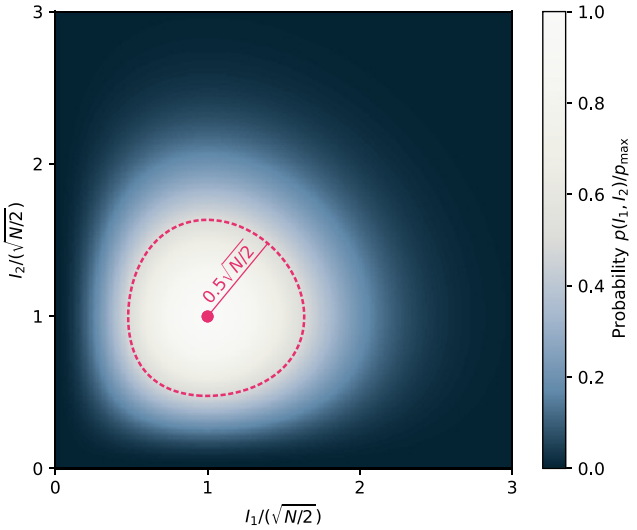

FIG. 7. Probability distribution of sampling an I_1, I_2 manifold in an infinite-temperature ensemble. The pink dashed curve represent a half-maximum contour of $\sqrt{N/2}$ diameter. The pink point represents the mode of the distribution at $I_1 = I_2 = \sqrt{N/2}$.

state purification and identical behavior of the central spin throughout the protocol.

However, the robustness of the optimized unitary gate sequence in the third stage of the protocol is expected to be more sensitive on sampled values of I_1 and I_2. This issue can be overcome by measurement postselection or measurement-based feed forward, provided the possibility of a single-shot readout of the central-spin state. For instance, measuring the transition rate asymmetry [23] of the $\Omega = \omega_1$ activated processes,

$$\begin{aligned} |\downarrow_x\rangle \left|I_1^z, I_2^z\right\rangle &\rightarrow |\uparrow_x\rangle \left|I_1^z - 1, I_2^z\right\rangle, \\ |\uparrow_x\rangle \left|I_1^z, I_2^z\right\rangle &\rightarrow |\downarrow_x\rangle \left|I_1^z + 1, I_2^z\right\rangle, \end{aligned} \tag{A2}$$

and the transition rate asymmetry of the $\Omega = \omega_2$ activated processes,

$$\begin{aligned} |\downarrow_x\rangle \left|I_1^z, I_2^z\right\rangle &\rightarrow |\uparrow_x\rangle \left|I_1^z, I_2^z - 1\right\rangle, \\ |\uparrow_x\rangle \left|I_1^z, I_2^z\right\rangle &\rightarrow |\downarrow_x\rangle \left|I_1^z, I_2^z + 1\right\rangle, \end{aligned} \tag{A3}$$

constrains both I_1 and I_2, which can be used to conditionally discard the postprotocol state or to adjust the gate parameters in the third stage of the protocol. Taking the example of GaAs QDs, where the noncollinear interaction results primarily from the electronic g-factor anisotropy [53] [yielding $\nu_i \sim \omega_i$ in Eq. (6)], telling apart the I_i and $I_i + 1$ manifolds in the suggested way would require resolving a $a/\sqrt{2I_i} \sim 2\pi \times 50$ kHz difference in transition rates of the activated processes, which is realistic given $\Gamma_{\text{deph}} = 2\pi \times 10$ kHz.

Moreover, if the proposed measures require too significant of an experimental overhead, the proof-of-concept experiments aimed at producing singletlike states, that is, lowering of the total angular momentum $\langle \mathbf{I}^2 \rangle$, can follow from the gate optimization performed in a larger portion of the Hilbert space (see Appendix E 3 d).

2. Breaking of the (I_1, I_2) conservation

On long timescales, the conservation of I_1 and I_2 is broken by processes resulting from intraensemble interactions (e.g., nuclear dipole-dipole interaction) or weak symmetry breaking resulting from small gradients in the single nucleus hyperfine constants. Under stage 2 of the protocol, the directionality of the imposed phase space flow towards an antipolarized state dictates that I_1 and I_2 will slowly increase under breaking of this conservation law (i.e., increased $|I_1^z|$ and $|I_2^z|$ can be accommodated only by higher I_1 and I_2 manifolds). This, in principle, could improve the protocol performance in two ways: firstly, by pushing the collective dynamics into the $I > \sqrt{N/2}$ regime, where they proceed faster, and secondly, by mitigating the effect of stochasticity in I_1 and I_2. Indeed, as soon as I_1 and I_2 reach values $> \sqrt{N/2}$, the degeneracies of the (I_1, I_2) manifolds start decreasing exponentially, with further increments in I_1 or I_2 (see Fig. 7).

Modeling these effects from first principles is beyond the scope of this work, as it requires a significant extension of the model and adds considerable complexity to the simulations. However, we argue that the models used throughout this work are sufficient to capture the resulting dynamics. Firstly, the increase in I_1 and I_2 results in the increase of collective enhancement factors, which could be entirely captured by working with a higher effective N. Secondly, the negative effects of intraensemble interactions and coupling inhomogeneities result in effective dephasing and spin diffusion, which are already represented in our model (albeit in a nonreversible, phenomenological way).

APPENDIX B: FULL SIMULATION OF QUANTUM DYNAMICS

To simulate the quantum dynamics of the composite system in a reduced Hilbert space, we use a master equation and steady-state solvers from the QuTiP [64,65] library in PYTHON.

The exchange between the central spin and the ensemble is modeled by the following Hamiltonian, written in a frame rotating with a δ-detuned laser drive, following a rotating-wave approximation:

$$\begin{aligned} H(t) = \Omega(t) S_x + \delta S_z + \sum_{i=1,2} \left(\omega_i - \frac{a^2}{4\omega_c}\right) I_i^z + \sum_{i=1,2} a S_z I_i^z \\ + \sum_{i,j=1,2} \frac{a^2}{4\omega_c} S_z (I_i^+ I_j^- + I_i^- I_j^+) + \sum_{i=1,2} \frac{a\nu_i}{2\omega_i} S_z I_i^x. \end{aligned} \tag{B1}$$

The individual terms are defined in the main text. We set $\Delta\omega = 1$ (arbitrary units) and from the value of κ used as an independent parameter obtain the corresponding three-body coupling strength ($a^2/4\omega_c$).

Within the first stage of the protocol setting $\Omega(t) = \omega_1$ [or $\Omega(t) = \omega_2$] activates the noncollinear ($\propto S_z I_i^x$) interaction. Within the second and third stages of the protocol, $\Omega(t) = \Delta\omega$ activates the three-body interaction [$\propto S_z(I_1^+ I_2^- + I_1^- I_2^+)$]. At all times, $\delta = 0$.

The instantaneous central-spin resets within the second stage of our protocol were effectuated by the following operation on the composite density operator:

$$\rho \to |{\downarrow_x}\rangle\langle{\downarrow_x}| \otimes \mathrm{Tr}_c \rho \tag{B2}$$

with Tr_c denoting the partial tracing with respect to the central-spin degrees of freedom.

The steady-state solver was applied to a continuous approximation of the protocol in which the central spin was reset continuously at an optical pumping rate $\Gamma_{\mathrm{op}} = 2\pi/\tau_0$, where τ_0 corresponds to the time between subsequent instantaneous central spin resets in the exact protocol. The collapse operator used in modeling that process was $\sqrt{\Gamma_{\mathrm{op}}}\,|{\downarrow_x}\rangle\langle{\uparrow_x}|$.

1. Dynamics in an $I_1 \neq I_2$ manifold

We verify the protocol robustness in an $I_1 \neq I_2$ manifold by performing an identical simulation to that from Sec. II D. Both κ and τ_0 are fixed to the same values, and the only difference lies in the choices of $I_1 = \sqrt{32/2} - 1$ and $I_2 = \sqrt{32/2} + 1$. The results are illustrated in Fig. 8, and organized in a one-to-one correspondence with those of Fig. 2 in the main text. As displayed in Fig. 8(a), the $\langle S_x\rangle$ population (that is, the only direct observable during the protocol) saturates to $-1/2$, as in Fig. 2(a). The polarizations I_1^z and I_2^z are driven towards the maximal possible opposite values, that is, $\pm\min(I_1, I_2)$ [see Fig. 8(c)], as anticipated. Dynamics features an equal amount of purification after settling to the limit cycle [see Fig. 8(d)], and the only significant difference comes in the degree of the $\langle \mathbf{I}^2\rangle$ reduction. Still, the protocol reaches the anticipated classical limit $\langle \mathbf{I}^2\rangle_{\mathrm{cl}} = (I_1 + I_2)(|I_1 - I_2| + 1)$.

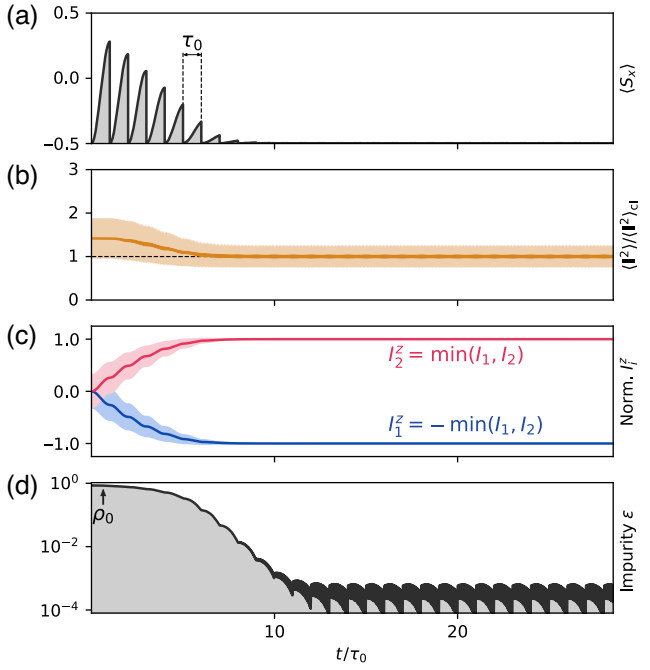

FIG. 8. Ideal system's dynamics for $N = 32$, and $I_1 = \sqrt{32/2} - 1$, $I_2 = \sqrt{32/2} + 1$. Panels (a)–(d) are in a one-to-one correspondence to those of Fig. 2 in the main text.

2. The effect of unequal species-specific hyperfine constants, $a_1 \neq a_2$

Here we justify the statement made in the main text that our choice to work with $a_1 = a_2$ does not lead to a loss of generality.

Suppose that we set $a_1 \neq a_2$. The first stage of the protocol would aim at minimizing the fluctuation of $a_1 I_1^z + a_1 I_2^z$ around the lock-point set by the detuning of the central-spin drive from ω_c [i.e., δ from the Hamiltonian in Eq. (B1)], whilst the second stage would push the state towards the edge of Hilbert space defined by the lower-I_i species reaching its maximal (or minimal) allowed spin projection, set by $|M| = \min(I_1, I_2)$. If these first two stages are alternated (i.e., run as a hybrid), the higher-I_i species is eventually found in a state that satisfies the condition $-\delta = a_1 I_1^z + a_2 I_2^z$. Note that, for $a_1 \neq a_2$, one could ensure that the higher-I_i species is also found in $|I_i^z| = M$, by setting $|\delta| = |a_1 - a_2|M$. If this value is expected to be large, δ can be chirped slowly, as in Ref. [23]. This explains why $a_1 \neq a_2$ does not change the physics behind the first two stages of the protocol.

If $a_1 \neq a_2$, the goal of the third stage of the protocol seems to be conceptually different: it is the magnitude of $(a_1\mathbf{I}_1 + a_2\mathbf{I}_2)^2$ that one should aim to minimize. However, expanding that expression, one quickly finds out that what needs to be minimized is $\mathbf{I}_1 \cdot \mathbf{I}_2 = \frac{1}{2}[(\mathbf{I}_1 + \mathbf{I}_2)^2 - I_1(I_1 + 1) - I_2(I_2 + 1)]$, that is, the total angular momentum squared: $(\mathbf{I}_1 + \mathbf{I}_2)^2$. The target state of the third preparation stage is—again—a many-body singlet (or, more generally, the state with $I = |I_1 - I_2|$). The final stage is executed in precisely the same way, although the broken harmonicity of the Jaynes-Cummings ladder may necessitate introducing a number of additional variational parameters: the Rabi frequencies of the central-spin drive $\{\Omega_i\}$.

3. Equal impact of the ensemble and the central-spin dephasing on the protocol's performance

We studied the effects of dephasing of the central spin and the ensemble on the protocol's performance. The

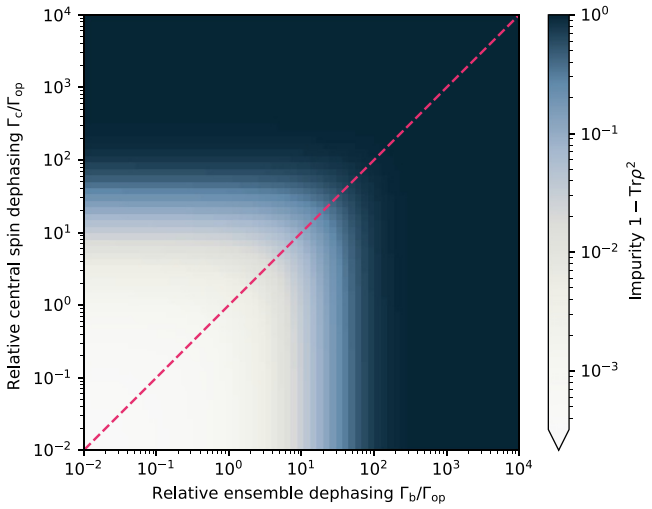

FIG. 9. Symmetry in the effect of ensemble and central-spin dephasing on the protocol's performance. The figure displays steady-state impurity as a function of relative ensemble and central-spin dephasing rates, $\Gamma_b/\Gamma_{\mathrm{op}}$ and $\Gamma_c/\Gamma_{\mathrm{op}}$. Here Γ_{op} denotes the optical pumping rate in the continuous quantum model. The simulation was run for $\kappa = 10$ and $N = 200$ (i.e., $I_1 = I_2 = \sqrt{200/2}$).

former process was modeled using a $\sqrt{\Gamma_c}S_x$ collapse operator, and the latter made use of two distinct collapse operators: $\sqrt{\Gamma_b/2}I_1^z$ and $\sqrt{\Gamma_b/2}I_2^z$. Figure 9 illustrates the steady-state impurity calculated in the continuous protocol approximation for a range of dephasing rates Γ_c and Γ_b. It is evident that both processes have quantitatively identical impact on the state preparation, which motivates introducing a total dephasing rate, $\Gamma_{\mathrm{deph}} = \Gamma_b + \Gamma_c$, as a figure of merit in quantifying resilience to the system's imperfections.

4. Effect of a τ chirp in the presence of spin diffusion

The effect of spin diffusion was studied numerically in the simulation of the pulsed protocol. This was incorporated into the model via the collapse operators

$$\sqrt{\Gamma_{\mathrm{diff}}}\sum_n |n\rangle\langle n+1|, \quad \sqrt{\Gamma_{\mathrm{diff}}}\sum_n |n\rangle\langle n-1|, \tag{B3}$$

with $|n\rangle$ representing the nth ladder state, $\left|I_1^z = -(M-n), I_2^z = +(M-n)\right\rangle$. Such operators relax the ensemble to a fully mixed state at rate Γ_{diff} in the absence of optical pumping.

In the analysis presented in Fig. 10, we chose $\Gamma_{\mathrm{diff}} = 0.1 \times 2\pi/(\tau_0\sqrt{N})$, and studied the cases in which $N = 32$, $N = 128$, and $N = 512$. The protocol with a fixed activation time, $\tau = \tau_0$, featured a decrease in robustness with

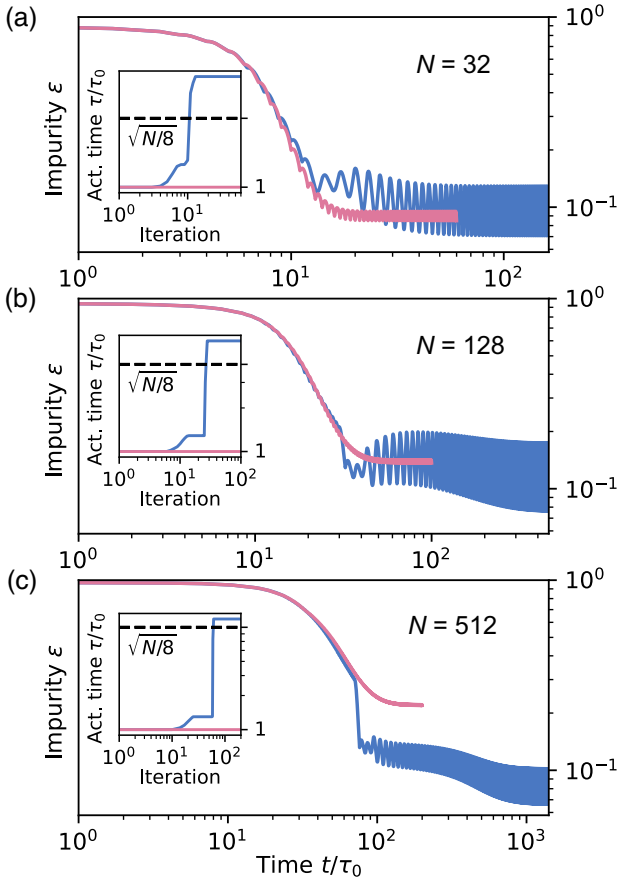

FIG. 10. Evolution of state impurity in the presence of spin diffusion: comparison of "fixed-τ" and "chirped-τ" protocols in systems of increasing size. Throughout the figure, the pink curves represent the evolution of state impurity, ϵ, in the antipolarization protocol with a fixed $\tau = \tau_0$, whereas the blue curves correspond to the "chirped-τ" protocols. The insets depict the corresponding τ-chirp profiles (color coding holds between the curves in the panels and the insets). Panels (a)–(c) correspond to the cases in which $N = 32$, $N = 128$, and $N = 512$, respectively. In all cases, $\Gamma_{\mathrm{diff}} = 0.1 \times 2\pi/(\tau_0\sqrt{N})$ and $\kappa = 10$.

an increase in N [see the pink curves in Figs. 10(a)–10(c)]. Such behavior is entirely expected: the flow down the ladder of states slows down due to an approximate $\sqrt{N}$ decrease in the collective enhancement rate of activated transitions. This effect becomes more pronounced as the system size N increases and in the presence of state-independent spin diffusion it has to be mitigated.

To this end, the activation time τ can be chirped from τ_0 up to about $\sqrt{N/8} \times \tau_0$, corresponding to the slowest interaction timescale in the system [cf. Eq. (E10) below]. The problem reduces to identifying the optimal chirp rate, which we achieve by conditioning the simulation to reset the central spin whenever the $d/dt\langle S_x\rangle = 0$ point is reached. Interestingly, this yields steplike chirp profiles, which are presented with blue curves in the insets of Figs. 10(a)–10(c). In practice, such chirp profiles would

have to be calibrated experimentally. The "chirped-τ" protocols exhibit consistent performance in all considered cases, as depicted with blue curves in Figs. 10(a)–10(c). The extension of the convergence time due to a τ chirp is—at most—by a factor $\sqrt{N}$.

The above approach is conceptually similar to that implemented experimentally in Ref. [16], in which the sensing time was gradually stepped in order to improve the feedback strength around the chosen total polarization lock point while overcoming the issue of the feedback's multistability.

APPENDIX C: RATE EQUATION MODEL

1. Evolution of populations and the scattering rates

A good quantitative understanding of the protocol dynamics can be gained from a simple rate equation model. Within this model, the dynamics is again restricted to the $I^z = 0$ ladder of states, as a result of perfect total polarization locking. The model assumes that at coarse-grained timescales, the coherences between different states across the ladder vanish, or in other words,

$$\mathrm{Tr}_c \rho = \sum_n p_n \, |n\rangle \, \langle n|. \tag{C1}$$

The evolution of the population of the $|n\rangle$ state, p_n, is then captured by the equation

$$\dot{p}_n = -(r_n^- + r_n^+)p_n + (r_{n-1}^+ p_{n-1} + r_{n+1}^- p_{n+1}), \tag{C2}$$

where $r_n^\pm$ stands for the rate of the population flow from the $|n\rangle$ state to the $|n \pm 1\rangle$ state.

The $\propto p_n$ terms in the equation describe the "out-flow" processes proceeding at a total rate $r_n^- + r_n^+$; see Fig. 11(a). In the absence of spin diffusion [the wavy yellow arrows in Figs. 11(a) and 11(b)], the first of the two processes ($\propto r_n^-$) involves a coherent exchange, $|\downarrow_x\rangle \, |n\rangle \to |\uparrow_x\rangle \, |n-1\rangle$, driven by the three-body interaction, and detuned by $\Delta_- = \Omega - \Delta\omega$, followed by the central-spin reset after time τ. Here, the reset is approximated as proceeding concomitantly with the exchange, at the optical pumping rate $\Gamma_{\mathrm{op}}(\tau) = 2\pi/\tau$. The second out-flow process ($\propto r_n^+$) consists of the same two steps, except that the dynamics proceeds between $|n\rangle$ and $|n+1\rangle$ states, for which the three-body interaction detuning is $\Delta_+ = \Omega + \Delta\omega$. The rates of the outflow processes, $r_n^\pm$, are then proportional to the populations of the excited states $|\uparrow_x\rangle \, |n \pm 1\rangle$, where the constants of proportionality are given by the central-spin reset rate, Γ_{op}. This yields

$$r_n^\pm = \Gamma_{\mathrm{op}} \langle |\uparrow_x, n \pm 1\rangle \, \langle \uparrow_x, n \pm 1| \rangle. \tag{C3}$$

We approximate the expectation value from Eq. (C3) by a steady-state excited-state population of a two-level system

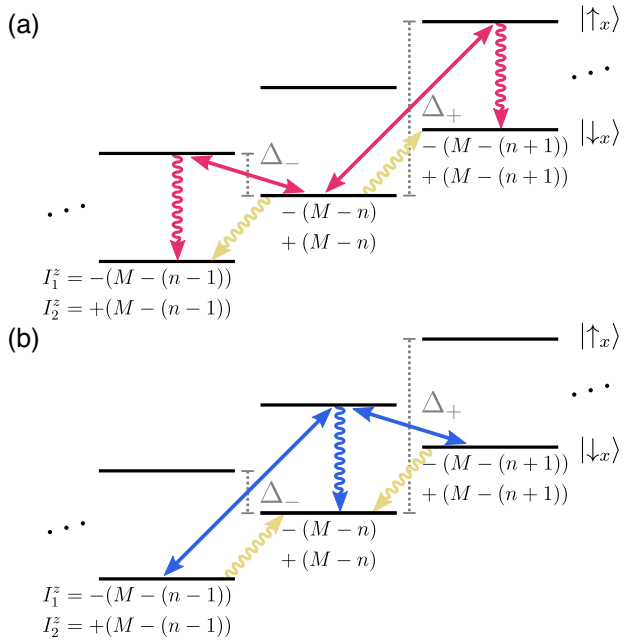

FIG. 11. Rate equation model of the protocol. (a) Scattering processes that depopulate the nth state across the ladder. Straight arrows denote activated three-body interactions, whereas gray bars show the energy gaps that suppress each of the processes. The pink wavy arrows illustrate the central spin resets, while the yellow wavy arrows illustrate the spin diffusion. (b) Scattering processes that populate the nth state across the ladder. Labeling is consistent with that of panel (a).

constituted by $|\downarrow_x, n\rangle$ and $|\uparrow_x, n \pm 1\rangle$ states; it follows that

$$r_n^\pm = \frac{\Gamma_{\mathrm{op}}}{2} \frac{(\alpha_n^\pm)^2/(\Gamma_{\mathrm{op}}\Gamma')}{1 + (\alpha_n^\pm)^2/(\Gamma_{\mathrm{op}}\Gamma') + (\Delta_\pm/\Gamma')^2}, \tag{C4}$$

where $\Gamma' = \frac{1}{2}\Gamma_{\mathrm{op}} + \Gamma_{\mathrm{deph}}$ incorporates the sum of phenomenological ensemble and central-spin dephasing rates, Γ_{deph}. The effective drive strengths, $\alpha_n^\pm$, correspond to the three-body interaction rate, given by

$$\begin{aligned} \alpha_n^+ &= \frac{a^2}{4\omega_c}(2I - n)(n+1), \\ \alpha_n^- &= \frac{a^2}{4\omega_c}(2I - n + 1)n. \end{aligned} \tag{C5}$$

Their dependence on I and n is a result of the collective enhancement, dependent on the total angular momenta of the subensembles ($I_1 = I_2 = I \sim \sqrt{N/2}$). Finally, to factor in the spin diffusion, proceeding at rate Γ_{diff}, the rates are modified as

$$r_n^\pm \to r_n^\pm + \Gamma_{\mathrm{diff}}. \tag{C6}$$

The second pair of terms in Eq. (C2) ($\propto p_{n-1}$ and $\propto p_{n+1}$) captures the effect of the "in-flow" processes.

The $|n\rangle$ state can be populated by a Δ_+-detuned process originating from the $|n-1\rangle$ state, a Δ_--detuned process originating from the $|n+1\rangle$ state, as well as the spin diffusion, as shown in Fig. 11(b). The relevant scattering rates are found using Eqs. (C4) and (C6).

Spin diffusion, in the considered form, drives the ensemble to a fully mixed state in the absence of optical pumping ($\Gamma_{\rm op}=0$).

2. Steady-state solution

The system reaches a steady state when $\dot{p}_n=0$ for all n. This generates the following recursive relation between the $|n\rangle$-state populations:

$$p_1=\frac{r_0^+}{r_1^-}p_0,$$
$$p_{n+2}=\frac{r_{n+1}^-+r_{n+1}^+}{r_{n+2}^-}p_{n+1}-\frac{r_n^+}{r_{n+2}^-}p_n,\quad n=0,1,\ldots,2I-2. \tag{C7}$$

This fully determines steady-state populations, up to a normalization factor, which can be constrained using $\sum_n p_n=1$.

The computational complexity of solving for steady-state populations is $\mathcal{O}(I)$; this is to be compared with $\mathcal{O}(I^6)$ complexity of solving for the steady state of the quantum master equation with dissipation.

3. Impurity ϵ in the presence of dephasing and spin diffusion: two regimes

The preparation performance can be characterized by the impurity of the reduced density operator, $\rho_b=\mathrm{Tr}_c\rho$. The rate equation model approximates this impurity by

$$\epsilon=1-\mathrm{Tr}\rho_b^2=1-\sum_n p_n^2. \tag{C8}$$

In the case of the perfect state preparation, we have $p_0=1$ and $\epsilon=0$. The preparation performance starts to drop when the $|1\rangle$ state acquires a finite population, leading to an initial impurity increase given by $\epsilon\approx 2r_0^+/r_1^-$. By the end of the chirp, the activation time τ is set to maximize r_1^- (see Appendix B 4), resulting in

$$r_1^-=\frac{\alpha}{\sqrt{2}}\frac{1}{2+\sqrt{2}\Gamma_{\rm deph}/\alpha}+\Gamma_{\rm diff},$$
$$r_0^+=\frac{\alpha}{\sqrt{2}}\frac{1}{2+\sqrt{2}\Gamma_{\rm deph}/\alpha+64\kappa^2N/(1+\sqrt{2}\Gamma_{\rm deph}/\alpha)}+\Gamma_{\rm diff}, \tag{C9}$$

where $\alpha=\alpha_0^+=\alpha_1^-$ [see Eq. (C5)]. The two terms in r_0^+ from Eq. (C9) represent two distinct physical mechanisms that limit the impurity: the directionality and the diffusion.

a. Diffusion-limited regime

If the first term of r_0^+ is negligible compared to $\Gamma_{\rm diff}$, the impurity is insensitive to κ. This defines a diffusion-limited regime in which the impurity scales as

$$\epsilon\approx\frac{8\mathcal{D}_{\rm diff}}{4\mathcal{D}_{\rm diff}+1}, \tag{C10}$$

where

$$\mathcal{D}_{\rm diff}=\left(1+\frac{\Gamma_{\rm deph}\tau_0\sqrt{N}}{2\pi}\right)\frac{\Gamma_{\rm diff}\tau_0\sqrt{N}}{2\pi}. \tag{C11}$$

b. Directionality-limited regime

If the first term of r_0^+ dominates $\Gamma_{\rm diff}$, the impurity is governed by κ, N, and $\Gamma_{\rm deph}\tau_0\sqrt{N}/2\pi$ in the following way:

$$\epsilon\approx\frac{2}{1+32N\kappa^2/\mathcal{D}_{\rm dir}} \tag{C12}$$

with

$$\mathcal{D}_{\rm dir}=\left(1+\frac{\Gamma_{\rm deph}\tau_0\sqrt{N}}{2\pi}\right)\left(1+2\frac{\Gamma_{\rm deph}\tau_0\sqrt{N}}{2\pi}\right). \tag{C13}$$

This defines a directionality-limited regime.

4. Convergence time T_c

The rate equation formalism allows us to estimate the convergence time of the protocol, T_c, from spectral analysis of matrix Λ, which generates the rate equation as

$$\dot{\mathbf{p}}=\Lambda\mathbf{p}, \tag{C14}$$

where $\mathbf{p}$ is a vector of $|n\rangle$-state populations.

We note that, due to the contractive nature of dynamics, the real parts of the Λ-matrix eigenvalues are all nonpositive, and can be arranged according to

$$0=\lambda_0>\mathrm{Re}(\lambda_1)>\mathrm{Re}(\lambda_2)>\cdots. \tag{C15}$$

We then identify $T_c=2\pi/|\mathrm{Re}(\lambda_1)|$, as $|\mathrm{Re}(\lambda_1)|$ is the slowest convergence rate in the model.

APPENDIX D: SURVEY OF CANDIDATE SYSTEMS

1. Relating the model spin diffusion rates to the measured depolarization timescales

To assess the performance of a candidate platform, the model spin diffusion rate between the ensemble's

TABLE I. Model parameters used to benchmark the protocol's performance for GaAs-AlGaAs QDs [25,52,66–68].

Total hyperfine interaction $A = N \times a$	$2\pi \times 11$ GHz
Zeeman frequency difference $\Delta\omega/B$	$2\pi \times 5.76$ MHz/T
Central-spin splitting ω_c/B	$2\pi \times 1.3$ GHz/T
Effective number of nuclei N	10^5
Dephasing rate (nuclear) Γ_{deph}	$2\pi \times 10$ kHz
Diffusion rate (nuclear) Γ_{diff}	$2\pi \times 125$ Hz
Magnetic field ranges B	1–10 T
Directionality parameter κ/B^2	6.2 T^{-2}
Activation time τ_0/B	2.2 μs/T
Reset time τ_r	1–10 ns

TABLE II. Model parameters used to benchmark the protocol's performance for InGaAs-GaAs QDs [26,50,68].

Total hyperfine interaction $A = N \times a$	$2\pi \times 11$ GHz
Zeeman frequency difference $\Delta\omega/B$	$2\pi \times 5.76$ MHz/T
Central-spin splitting ω_c/B	$2\pi \times 6$ GHz/T
Effective number of nuclei N	10^5
Dephasing rate (nuclear) Γ_{deph}	$2\pi \times 10$ MHz
Diffusion rate (nuclear) Γ_{diff}	$2\pi \times 15$ Hz
Magnetic field ranges B	100 mT–10 T
Directionality parameter κ/B^2	28.6 T^{-2}
Activation time τ_0/B	9.9 μs/T
Reset time τ_r	1–10 ns

TABLE III. Model parameters used to benchmark the protocol's performance for gate-defined GaAs QDs [15,48,59,67,68].

Total hyperfine interaction $A = N \times a$	$2\pi \times 11$ GHz
Zeeman frequency difference $\Delta\omega/B$	$2\pi \times 5.76$ MHz/T
Central-spin splitting ω_c/B	$2\pi \times 8$ GHz/T
Effective number of nuclei N	10^6
Dephasing rate (nuclear) Γ_{deph}	$2\pi \times 10$ kHz
Diffusion rate (nuclear) Γ_{diff}	$2\pi \times 76$ kHz
Magnetic field ranges B	100 mT–10 T
Directionality parameter κ/B^2	380.8 T^{-2}
Activation time τ_0/B	132.2 μs/T
Reset time τ_r	100 ns

macrostates, Γ_{diff}, has to be linked to a more direct platform-specific relaxation timescale, like that of the polarization loss: T_1^{pol}.

In this analysis, we assume that the polarization-dependent relaxation rates between the two polarization macrostates (in the units of angular frequency) are well approximated [47] by

$$\Gamma_{\text{diff}}^{\pm}(I_i^z) = 2\pi \times \frac{1}{2T_1^{\text{pol}}}\left(\frac{N}{2} \mp I_i^z\right), \tag{D1}$$

where the "±" superscript corresponds to the $I_i^z \to I_i^z \pm 1$ relaxation. The directionality native to the resulting Ornstein-Uhlenbeck depolarization process is intuitive: an almost fully polarized ensemble is far more likely to depolarize than to polarize via a random spin flip. In this model, the ensemble features a polarization loss given by $\langle I_i^z(t)\rangle = e^{-t/T_1^{\text{pol}}}(N/2)$, as it settles into a steady state with $p(I_i^z) \propto e^{-(I_i^z)^2/2\Delta^2 I_i^z}$. Here, $\sqrt{\Delta^2 I_i^z} = \sqrt{N}/2$, in full agreement with the infinite-temperature result.

In the vicinity of $|I_1^z|, |I_2^z| \sim \sqrt{N} \ll N$, where the antipolarization protocol takes place,

$$\Gamma_{\text{diff}}^{+}(I_i^z) \approx \Gamma_{\text{diff}}^{-}(I_i^z) \approx \text{const.}, \tag{D2}$$

recovering purely diffusive dynamics, as considered in the rate equation model (see Appendix C). We therefore link the model diffusion rate to the depolarization timescale as follows:

$$\Gamma_{\text{diff}} = 2\pi \times \frac{N}{4T_1^{\text{pol}}}. \tag{D3}$$

In our platform-specific analysis, we calculate Γ_{diff} using the above formula in the case of all types of QDs. In the case of REIs, Γ_{diff} is measured directly in Ref. [19] as the lifetime of the fully polarized state.

2. Tables of physical parameters

The physical parameters used to benchmark the performance of the candidate material platforms presented in Figs. 4–6 are listed in Tables I–IV.

APPENDIX E: OPTIMIZING THE PREPARATION OF A MANY-BODY SINGLET

1. Central-spin gate

We introduce the following notation for a single-qubit gate:

$$(\phi)_j \equiv \exp\{-i\phi\sigma_j/2\}, \qquad j = x, y, z, \tag{E1}$$

TABLE IV. Model parameters used to benchmark the protocol's performance for a $^{171}\text{Yb}^{3+} : \text{YVO}_4$ (REI) [19,60]. The three-body interaction in this system is a central-spin-mediated second-order dipole-dipole, and it couples the nuclei in the second shell (subscript i) with those in the outer (subscript j) shells with an effective strength of about $a_i a_j/\omega_c$. The $\Delta\omega$ corresponds to the difference in quadrupolar frequencies of the nuclei in the second shell (i.e., a frozen core) and the outer shells.

Three-body interaction strength $a_i a_j/\omega_c$	$2\pi \times 0.1$ kHz
Quadrupolar frequency difference $\Delta\omega$	$2\pi \times 10$–100 kHz
Directionality parameter κ	25–250
Number of nuclei	4
Dephasing rate Γ_{deph}	$2\pi \times 1.25$ kHz
Diffusion rate Γ_{diff}	$2\pi \times 1.85$ Hz
Activation time τ_0	5 ms
Reset time τ_r	500 μs

with σ_x, σ_y, and σ_z 2×2 Pauli matrices.

2. Three-body interaction gate

Upon matching the $\Omega = \Delta\omega$ resonance condition, the evolution of the system in the frame rotating with $\frac{1}{2}\Delta\omega(I_1^z - I_2^z) + \Omega S_x$ is dictated by the Hamiltonian

$$H_{\mathrm{exc}} = \frac{a^2}{4\omega_c}(|\uparrow_x\rangle\langle\downarrow_x|\mathcal{I}_- + |\downarrow_x\rangle\langle\uparrow_x|\mathcal{I}_+), \tag{E2}$$

where $\mathcal{I}_\pm = I_1^\pm I_2^\mp$ are the nonlinear ladder operators for the effective Jaynes-Cummings ladder of $|n\rangle$ states, whose action is captured by

$$\mathcal{I}_+ = \sum_{n=0}^{2I-1} \underbrace{(2I-n)(n+1)}_{e_n} |n+1\rangle\langle n| \tag{E3}$$

and $\mathcal{I}_- = (\mathcal{I}_+)^\dagger$.

Evolution of the system in that frame over time τ, generated by H_{exc}, realizes the gate

$$\begin{aligned}
&\exp\{-i\tau H_{\mathrm{exc}}\} \\
&= \mathbb{1} + |\uparrow_x\rangle\langle\uparrow_x| \otimes \sum_{n=0}^{2I-1}\left(\cos\frac{a^2 e_n \tau}{4\omega_c} - 1\right)|n\rangle\langle n| \\
&+ |\downarrow_x\rangle\langle\downarrow_x| \otimes \sum_{n=0}^{2I-1}\left(\cos\frac{a^2 e_n \tau}{4\omega_c} - 1\right)|n+1\rangle\langle n+1| \\
&- |\uparrow_x\rangle\langle\downarrow_x| \otimes \sum_{n=0}^{2I-1} i\sin\frac{a^2 e_n \tau}{4\omega_c}|n\rangle\langle n+1| \\
&- |\downarrow_x\rangle\langle\uparrow_x| \otimes \sum_{n=0}^{2I-1} i\sin\frac{a^2 e_n \tau}{4\omega_c}|n+1\rangle\langle n|\,.
\end{aligned} \tag{E4}$$

In particular, it is readily seen that the exact π-gate time, τ_π, is dependent on n since the enhancement factors e_n vary across the ladder of states.

In contrast, for the simplified system with $e_n = \mathrm{const.}$, the exchange interaction π gate would be

$$\begin{aligned}
&\exp\{-i\tau_\pi H_{\mathrm{exc}}^0\} \\
&= |\downarrow_x\rangle\langle\downarrow_x| \otimes |0\rangle\langle 0| + |\uparrow_x\rangle\langle\uparrow_x| \otimes |2I\rangle\langle 2I| \\
&\quad - i|\uparrow_x\rangle\langle\downarrow_x| \sum_{n=0}^{2I-1} |n\rangle\langle n+1| - i|\downarrow_x\rangle\langle\uparrow_x| \\
&\quad \times \sum_{n=0}^{2I-1} |n+1\rangle\langle n|\,.
\end{aligned} \tag{E5}$$

3. Optimizing the gates via gradient descent

In order to tailor the sequence parameters in a real system, we minimize the appropriately constructed cost function, which takes the quantum state

$$|\psi\rangle = \overleftarrow{\prod_{j=0}}(\exp\{-i\tau_j H_{\mathrm{exc}}\}\exp\{-i\phi_j\sigma_z/2\})\,|\downarrow_x\rangle \otimes |n=0\rangle \tag{E6}$$

as an input (a method originally devised in Ref. [55]). The arrow over the product sign represents direction of stacking the consecutive terms with $j = 0, 1, 2, \ldots$ in the product. The minimization is done with respect to the variational parameters $\{\tau_j, \phi_j\}_{j=0,1,2,\ldots}$, which correspond directly to the three-body interaction activation times (τ_j), and phases of central-spin gates (ϕ_j). To reach the minimum of the cost function, we apply the RMSprop gradient descent algorithm in the space of $\{\tau_j, \phi_j\}_{j=0,1,2,\ldots}$.

a. Choice of the cost function

We choose a Hilbert-Schmidt distance between the singlet state, $\chi = |I=0\rangle\langle I=0|$, and the reduced density operator of the ensemble, $\rho_b = \mathrm{Tr}_c(|\psi\rangle\langle\psi|)$, as our cost function:

$$\mathcal{C}(|\psi\rangle) = \mathrm{Tr}(\rho_b - \chi)^\dagger(\rho_b - \chi). \tag{E7}$$

The main advantage of working with this cost function is an ease of calculating its gradient analytically, which speeds up the optimization procedure. To see it, we first act with the differential operator, on the $|\psi\rangle$ state from Eq. (E6), and find

$$\begin{aligned}
\partial_{v_i}|\psi\rangle &= \left(\overleftarrow{\prod_{j>i}} e^{-iv_j X_j}\right)(-iX_i e^{-iv_i X_i}) \\
&\quad \times \left(\overleftarrow{\prod_{j<i}} e^{-iv_j X_j}\right)|\downarrow_x\rangle \otimes |n=0\rangle
\end{aligned} \tag{E8}$$

for variational parameters $v_j \in \{\tau_j, \phi_j\}$ and operators $X_j \in \{H_{\mathrm{exc}}, \sigma_z/2\}$. We then note that extending this result to the cost function from Eq. (E7) amounts to a simple application of a chain rule.

b. Hyperparameters and convergence of an RMSprop algorithm

The update rule for a given variational parameter, v, in our implementation of the RMSprop algorithm is

$$\begin{aligned}
v_{i+1} &= v_i - \frac{\zeta}{\sqrt{\xi + \mathbb{E}_i[(\partial_v\mathcal{C})^2]}} \times [\partial_v\mathcal{C}]_i, \\
\mathbb{E}_i[(\partial_v\mathcal{C})^2] &= \beta\mathbb{E}_{i-1}[(\partial_v\mathcal{C})^2] + (1-\beta)[\partial_v\mathcal{C}]_i^2,
\end{aligned} \tag{E9}$$

where $\partial_v\mathcal{C}$ is the partial derivative of the cost function $\mathcal{C}$

with respect to the variational parameter v. The hyperparameters used throughout the optimization routines were $\zeta = 0.015$, $\xi = 10^{-8}$, and $\beta = 0.85$.

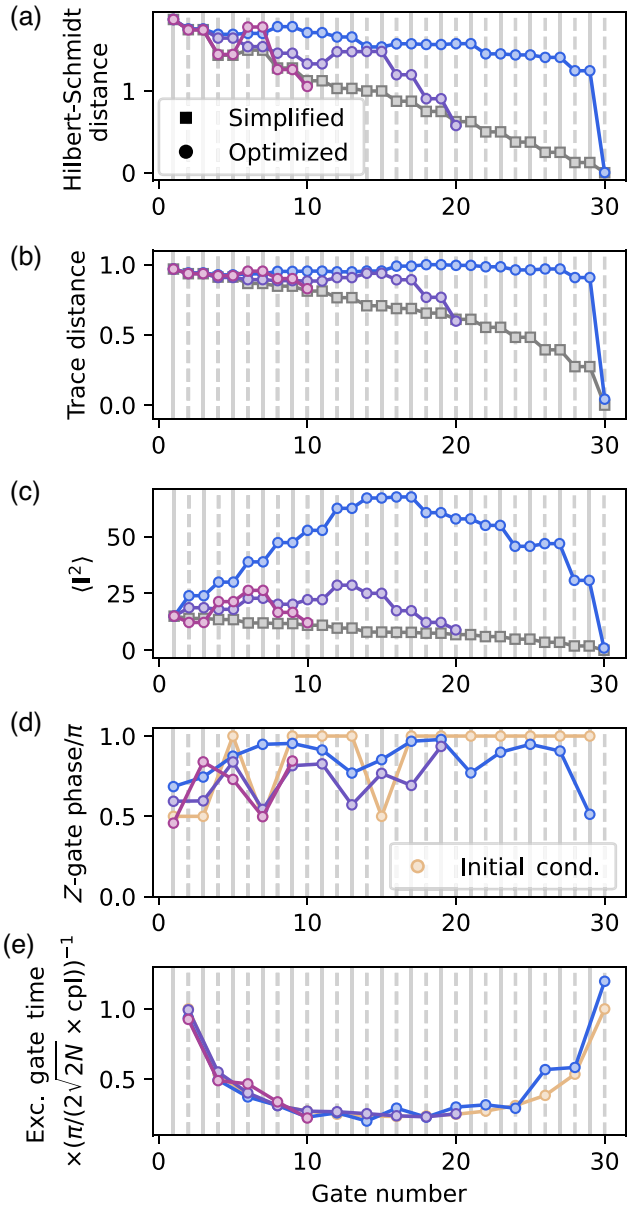

FIG. 12. Optimizing gate times and phases for singlet preparation. (a) Hilbert-Schmidt distance (i.e., our cost function $\mathcal{C}$) during simplified (squares) and optimized (circles) protocols of varied length. The color coding is consistent with Fig. 6(c) of the main text, which only concerns the protocols' endpoints. (b) Evolution of the trace distance in considered protocols. (c) Evolution of the expectation value of total angular momentum squared in the considered protocols. (d) Optimal Z-gate phases in protocols of varied length. The beige circles correspond to the initial condition for the gradient descent optimization. (e) Optimal exchange gate times in protocols of varied length. The beige circles correspond to the initial condition for the gradient descent optimization. Here "cpl" stands for the coupling strength, $a^2/(4\omega_c)$.

For all the sequences of lengths shorter than the maximal considered, the convergence was reached in less than 1000 optimization epochs. For the longest considered sequence, optimization was terminated after 7000 epochs; however, the cost function could likely be decreased further. The difficulty of this task comes most likely from the presence of a barren plateau in a cost function landscape—i.e., region around the minimum, where the gradients of $\mathcal{C}$ vanish exponentially fast [69].

The evolutions of the cost function $\mathcal{C}$, the trace distance, and the expectation value of total angular momentum squared during the optimal protocols of varied length are plotted in Figs. 12(a), 12(b), 12(c), respectively (circles). Their simplified system counterparts are plotted alongside for reference (squares).

c. Initial condition for gradient descent

To speed up the convergence of the gradient descent optimization, we start the procedure with a physically motivated initial guess for variational parameters.

The initial z-gate phases are chosen to be identical to those in the optimal protocol for the idealized system [see the main text, and the beige circles in Fig. 12(d)].

The initial activation times for the three-body interaction are chosen as

$$\tau_j = \pi / \left(2e_j \times \frac{a^2}{4\omega_c} \right), \tag{E10}$$

where e_j stands for the enhancement factor from Eq. (E3); see the beige circles in Fig. 12(e). The intuition behind this choice is that it realizes the ideal amplitude transfer for each consecutive $|n\rangle$ state brought into the superposition.

d. Manifold-averaged gradient descent

In the main text, the many-body singlet preparation sequence was found assuming that the dynamics is constrained to the $I_1 = I_2 = \sqrt{N/2}$ manifold. Realizing such a scenario requires the measurement of I_1 and I_2, e.g., via postselection (see Appendix A). Here, we develop an alternative near-term strategy that does not require such experimental overhead and that can serve as a robust proof-of-concept way to suppress the magnitude of the total angular momentum of the ensemble: $\langle \mathbf{I}^2 \rangle$.

We perform a variational optimization over all likely values of I_1 and I_2 at once. The state of the ensemble at the beginning of the protocol is taken as

$$\rho_n^0 = \sum_{I_1,I_2} w_{I_1,I_2} \left| +M_{I_1,I_2}, -M_{I_1,I_2} \right\rangle \left\langle +M_{I_1,I_2}, -M_{I_1,I_2} \right| \tag{E11}$$

with

$$w_{I_1,I_2} = \left(\frac{1}{2^N}\right)^2 \frac{N!(2I_1+1)^2}{(N/2+I_1+1)!(N/2-I_1)!} \times \frac{N!(2I_2+1)^2}{(N/2+I_2+1)!(N/2-I_2)!} \tag{E12}$$

standing for the (I_1, I_2)-manifold weights calculated exactly, away from the large-N limit (cf. Appendix A). This is equivalent to the assumption that the first two stages of the protocol work perfectly in all considered (I_1, I_2) manifolds, yielding a mixture of pure antipolarized states with $M_{I_1,I_2} = \min(I_1, I_2)$.

A natural choice for the cost function is then

$$\mathcal{C} = \mathrm{Tr}_n(\rho_n \mathbf{I}^2) \tag{E13}$$

with $\rho_n = \mathrm{Tr}_c(U_{\mathrm{tot}} |{\downarrow_x}\rangle \langle{\downarrow_x}| \rho_n^0 U_{\mathrm{tot}}^\dagger)$, where U_{tot} represents the sequence of unitary gates comprising the final stage of the protocol.

To assess the protocol's robustness in lowering $\langle \mathbf{I}^2 \rangle$ in the considered scenario, we adapt the classical bound on $\langle \mathbf{I}^2 \rangle$ reduction as

$$\overline{\langle \mathbf{I}^2 \rangle}_{\mathrm{cl}} = \sum_{I_1,I_2} w_{I_1,I_2} \langle \mathbf{I}^2 \rangle_{\mathrm{cl}} = \sum_{I_1,I_2} w_{I_1,I_2} (I_1+I_2)(|I_1-I_2|+1), \tag{E14}$$

and, similarly, the quantum bound on $\langle \mathbf{I}^2 \rangle$ reduction as

$$\overline{\langle \mathbf{I}^2 \rangle}_{\mathrm{qu}} = \sum_{I_1,I_2} w_{I_1,I_2} \langle \mathbf{I}^2 \rangle_{\mathrm{qu}} = \sum_{I_1,I_2} w_{I_1,I_2} |I_1-I_2|(|I_1-I_2|+1). \tag{E15}$$

Note that in the scenario where I_1 and I_2 can vary, $\overline{\langle \mathbf{I}^2 \rangle}_{\mathrm{qu}} > 0$, and therefore the exact preparation of a many-body singlet is not feasible. However, a significant reduction below the classical bound is still possible.

Figure 13(a) shows the evolution of the cost function with increasing sequence length for $K = 2, 3$, and 4. In contrast to the case of engineering the many-body singlet (main text), the implemented sequences display a much faster initial convergence with an exponential decay towards the cost function minima with an increase in the sequence lengths: a remarkable feature that raises hope of near-term proof-of-concept experiments. The optimal gate phases for the $K = 4$ case and for a sequence length of 26 are plotted in Fig. 13(b). The corresponding gate times are displayed in Fig. 13(c).

The gradient descent optimizer implements the same RMSprop algorithm (and uses the same hyperparameters, as well as the preconditioning) as the optimizer for the sequences considered in the main text. The convergence of the sequence parameters was reached in less than 5000 optimization epochs, regardless of the value of K or the sequence length.

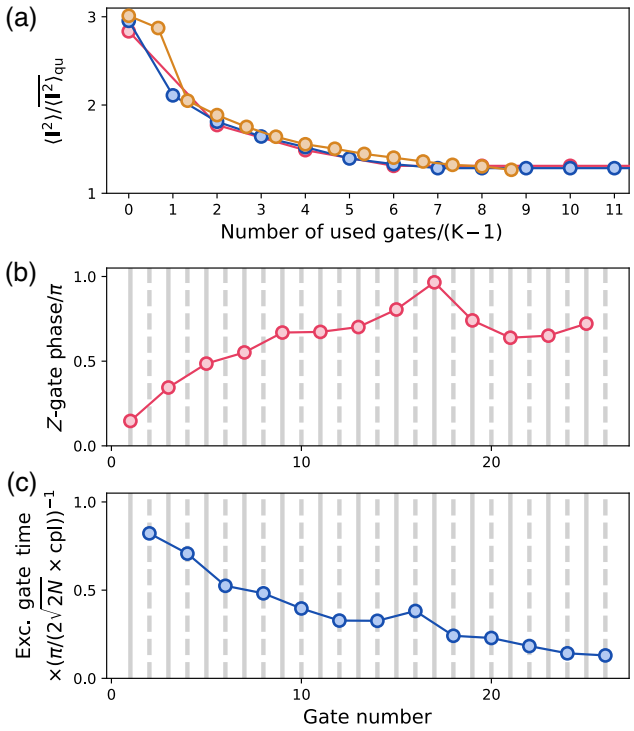

FIG. 13. Optimizing gate times and phases for manifold-averaged total angular momentum reduction. (a) Manifold-averaged total angular momenta (normalized by the quantum limit) as a function of the number of gates used (normalized by $K-1$) for $K = 2$ (red dots), $K = 3$ (blue dots), and $K = 4$ (yellow dots). For each K, the point representative of 0 gates used displays $\overline{\langle \mathbf{I}^2 \rangle}_{\mathrm{cl}}/\overline{\langle \mathbf{I}^2 \rangle}_{\mathrm{qu}}$. (b) Optimal Z-gate phases in the protocol with 26 gates ($K = 4$). (c) Optimal exchange gate times in the protocol with 26 gates ($K = 4$). Here "cpl" stands for the coupling strength, $a^2/(4\omega_c)$.

Interestingly, the identified sequences bias the importance of $I_1 \neq I_2$ manifolds, based on their large contributions to $\langle \mathbf{I}^2 \rangle$. The fact that simultaneous optimization in these manifolds is so robust could be explained by the addition of classical angular momenta: it is $1/(1-\sqrt{3}/2) \approx 7.5$ times more likely to reduce the total angular momentum when adding randomly oriented, unbalanced ($I_1 \ll I_2$) angular momenta than when adding balanced ($I_1 \sim I_2$) momenta.

4. Singlet autorefocusing in a nonrotating frame

A singlet state prepared in the frame rotating with $\frac{1}{2}\Delta\omega(I_1^z - I_2^z) + \Omega S_x$ will coincide with a singlet state in a nonrotating frame at times $t = 2\pi k/\Delta\omega$ for $k = 0, 1, 2, 3, \ldots$; indeed, in a nonrotating frame the evolution

of the prepared state (up to a global phase) is given by

$$|\psi(t)\rangle = |\downarrow_x\rangle \otimes \sum_{n=0}^{2I} \frac{(-1)^n}{\sqrt{2I+1}} \exp\{itn\Delta\omega\}\,|n\rangle. \quad \text{(E16)}$$

[1] E. Takou, E. Barnes, and S. E. Economou, Precise control of entanglement in multinuclear spin registers coupled to defects, Phys. Rev. X **13**, 011004 (2023).

[2] D. P. DiVincenzo, The physical implementation of quantum computation, Fortschritte der Phys. **48**, 771 (2000).

[3] D. J. Wineland, Nobel Lecture: Superposition, entanglement, and raising Schrödinger's cat, Rev. Mod. Phys. **85**, 1103 (2013).

[4] E. M. Kessler, G. Giedke, A. Imamoglu, S. F. Yelin, M. D. Lukin, and J. I. Cirac, Dissipative phase transition in a central spin system, Phys. Rev. A **86**, 012116 (2012).

[5] C.-E. Bardyn and A. Imamoglu, Majorana-like modes of light in a one-dimensional array of nonlinear cavities, Phys. Rev. Lett. **109**, 253606 (2012).

[6] J. Marino, Y. E. Shchadilova, M. Schleier-Smith, and E. A. Demler, Spectrum, Landau–Zener theory and driven-dissipative dynamics of a staircase of photons, New J. Phys. **21**, 013009 (2019).

[7] Q. Chen, I. Schwarz, and M. B. Plenio, Steady-state preparation of long-lived nuclear spin singlet pairs at room temperature, Phys. Rev. B **95**, 224105 (2017).

[8] J. N. Greiner, D. B. R. Dasari, and J. Wrachtrup, Purification of an unpolarized spin ensemble into entangled singlet pairs, Sci. Rep. **7**, 529 (2017).

[9] T. N. Ikeda and M. Sato, General description for nonequilibrium steady states in periodically driven dissipative quantum systems, Sci. Adv. **6**, abb4019 (2020).

[10] M. Issler, E. M. Kessler, G. Giedke, S. Yelin, I. Cirac, M. D. Lukin, and A. Imamoglu, Nuclear spin cooling using Overhauser-field selective coherent population trapping, Phys. Rev. Lett. **105**, 267202 (2010).

[11] G. Éthier-Majcher, D. Gangloff, R. Stockill, E. Clarke, M. Hugues, C. Le Gall, and M. Atatüre, Improving a solid-state qubit through an engineered mesoscopic environment, Phys. Rev. Lett. **119**, 130503 (2017).

[12] N. Behbood, G. Colangelo, F. Martin Ciurana, M. Napolitano, R. J. Sewell, and M. W. Mitchell, Feedback cooling of an atomic spin ensemble, Phys. Rev. Lett. **111**, 103601 (2013).

[13] B. Zhu, J. Marino, N. Y. Yao, M. D. Lukin, and E. A. Demler, Dicke time crystals in driven-dissipative quantum many-body systems, New J. Phys. **21**, 073028 (2019).

[14] B. Urbaszek, X. Marie, T. Amand, O. Krebs, P. Voisin, P. Maletinsky, A. Högele, and A. Imamoglu, Nuclear spin physics in quantum dots: An optical investigation, Rev. Mod. Phys. **85**, 79 (2013).

[15] H. Bluhm, S. Foletti, I. Neder, M. Rudner, D. Mahalu, V. Umansky, and A. Yacoby, Dephasing time of GaAs electron-spin qubits coupled to a nuclear bath exceeding 200 μs, Nat. Phys. **7**, 109 (2011).

[16] D. M. Jackson, U. Haeusler, L. Zaporski, J. H. Bodey, N. Shofer, E. Clarke, M. Hugues, M. Atatüre, C. Le Gall, and D. A. Gangloff, Optimal purification of a spin ensemble by quantum-algorithmic feedback, Phys. Rev. X **12**, 031014 (2022).

[17] D. M. Jackson, D. A. Gangloff, J. H. Bodey, L. Zaporski, C. Bachorz, E. Clarke, M. Hugues, C. Le Gall, and M. Atatüre, Quantum sensing of a coherent single spin excitation in a nuclear ensemble, Nat. Phys. **17**, 585 (2021).

[18] I. Schwartz, J. Scheuer, B. Tratzmiller, S. Müller, Q. Chen, I. Dhand, Z.-Y. Wang, C. Müller, B. Naydenov, F. Jelezko, and M. B. Plenio, Robust optical polarization of nuclear spin baths using Hamiltonian engineering of nitrogen-vacancy center quantum dynamics, Sci. Adv. **4**, eaat8978 (2018).

[19] A. Ruskuc, C.-J. Wu, J. Rochman, J. Choi, and A. Faraon, Nuclear spin-wave quantum register for a solid-state qubit, Nature **602**, 408 (2022).

[20] H. P. Bartling, M. H. Abobeih, B. Pingault, M. J. Degen, S. J. H. Loenen, C. E. Bradley, J. Randall, M. Markham, D. J. Twitchen, and T. H. Taminiau, Entanglement of spin-pair qubits with intrinsic dephasing times exceeding a minute, Phys. Rev. X **12**, 011048 (2022).

[21] M. H. Abobeih, Y. Wang, J. Randall, S. J. H. Loenen, C. E. Bradley, M. Markham, D. J. Twitchen, B. M. Terhal, and T. H. Taminiau, Fault-tolerant operation of a logical qubit in a diamond quantum processor, Nature **606**, 884 (2022).

[22] D. A. Gangloff, G. Éthier Majcher, C. Lang, E. V. Denning, J. H. Bodey, D. M. Jackson, E. Clarke, M. Hugues, C. Le Gall, and M. Atatüre, Quantum interface of an electron and a nuclear ensemble, Science **364**, 62 (2019).

[23] D. A. Gangloff, L. Zaporski, J. H. Bodey, C. Bachorz, D. M. Jackson, G. Éthier-Majcher, C. Lang, E. Clarke, M. Hugues, C. Le Gall, and M. Atatüre, Witnessing quantum correlations in a nuclear ensemble via an electron spin qubit, Nat. Phys. **17**, 1247 (2021).

[24] G. Wüst, M. Munsch, F. Maier, A. V. Kuhlmann, A. Ludwig, A. D. Wieck, D. Loss, M. Poggio, and R. J. Warburton, Role of the electron spin in determining the coherence of the nuclear spins in a quantum dot, Nat. Nanotechnol. **11**, 885 (2016).

[25] L. Zaporski, N. Shofer, J. H. Bodey, S. Manna, G. Gillard, D. M. Jackson, M. H. Appel, C. Schimpf, S. C. da Silva, J. Jarman, G. Delamare, G. Park, U. Haeusler, E. A. Chekhovich, A. Rastelli, D. A. Gangloff, M. Atatüre, and C. Le Gall, Ideal refocusing of an optically active spin qubit under strong hyperfine interactions (2022).

[26] R. Stockill, C. Le Gall, C. Matthiesen, L. Huthmacher, E. Clarke, M. Hugues, and M. Atatüre, Quantum dot spin coherence governed by a strained nuclear environment, Nat. Commun. **7**, 12745 (2016).

[27] J. Randall, C. E. Bradley, F. V. van der Gronden, A. Galicia, M. H. Abobeih, M. Markham, D. J. Twitchen, F. Machado, N. Y. Yao, and T. H. Taminiau, Many-body-localized discrete time crystal with a programmable spin-based quantum simulator, Science **374**, 1474 (2021).

[28] A. Browaeys and T. Lahaye, Many-body physics with individually controlled Rydberg atoms, Nat. Phys. **16**, 132 (2020).

[29] N. Behbood, F. Martin Ciurana, G. Colangelo, M. Napolitano, G. Tóth, R. J. Sewell, and M. W. Mitchell, Generation of macroscopic singlet states in a cold atomic ensemble, Phys. Rev. Lett. **113**, 093601 (2014).

[30] R. McConnell, H. Zhang, J. Hu, S. Ćuk, and V. Vuletić, Entanglement with negative Wigner function of almost 3,000 atoms heralded by one photon, Nature **519**, 439 (2015).

[31] Z. Li, B. Braverman, S. Colombo, C. Shu, A. Kawasaki, A. F. Adiyatullin, E. Pedrozo-Peñafiel, E. Mendez, and V. Vuletić, Collective spin-light and light-mediated spin-spin interactions in an optical cavity, PRX Quantum **3**, 020308 (2022).

[32] G. Tóth and M. W Mitchell, Generation of macroscopic singlet states in atomic ensembles, New J. Phys. **12**, 053007 (2010).

[33] A. Reiserer, N. Kalb, M. S. Blok, K. J. M. van Bemmelen, T. H. Taminiau, R. Hanson, D. J. Twitchen, and M. Markham, Robust quantum-network memory using decoherence-protected subspaces of nuclear spins, Phys. Rev. X **6**, 021040 (2016).

[34] S. J. DeVience, R. L. Walsworth, and M. S. Rosen, Preparation of nuclear spin singlet states using spin-lock induced crossing, Phys. Rev. Lett. **111**, 173002 (2013).

[35] C. Zu, F. Machado, B. Ye, S. Choi, B. Kobrin, T. Mittiga, S. Hsieh, P. Bhattacharyya, M. Markham, D. Twitchen, A. Jarmola, D. Budker, C. R. Laumann, J. E. Moore, and N. Y. Yao, Emergent hydrodynamics in a strongly interacting dipolar spin ensemble, Nature **597**, 45 (2021).

[36] A. Högele, M. Kroner, C. Latta, M. Claassen, I. Carusotto, C. Bulutay, and A. Imamoglu, Dynamic nuclear spin polarization in the resonant laser excitation of an InGaAs quantum dot, Phys. Rev. Lett. **108**, 197403 (2012).

[37] W. Yang and L. J. Sham, General theory of feedback control of a nuclear spin ensemble in quantum dots, Phys. Rev. B **88**, 235304 (2013).

[38] E. A. Chekhovich, A. Ulhaq, E. Zallo, F. Ding, O. G. Schmidt, and M. S. Skolnick, Measurement of the spin temperature of optically cooled nuclei and GaAs hyperfine constants in GaAs/AlGaAs quantum dots, Nat. Mater. **16**, 982 (2017).

[39] J. M. Taylor, A. Imamoglu, and M. D. Lukin, Controlling a mesoscopic spin environment by quantum bit manipulation, Phys. Rev. Lett. **91**, 246802 (2003).

[40] M. S. Rudner, L. M. K. Vandersypen, V. Vuletić, and L. S. Levitov, Generating entanglement and squeezed states of nuclear spins in quantum dots, Phys. Rev. Lett. **107**, 206806 (2011).

[41] R. H. Dicke, Coherence in spontaneous radiation processes, Phys. Rev. **93**, 99 (1954).

[42] H. Sun, P. Xu, H. Pu, and W. Zhang, Efficient generation of many-body singlet states of spin-1 bosons in optical superlattices, Phys. Rev. A **95**, 063624 (2017).

[43] W. A. Coish, J. Fischer, and D. Loss, Exponential decay in a spin bath, Phys. Rev. B **77**, 125329 (2008).

[44] Ł. Cywiński, W. M. Witzel, and S. Das Sarma, Pure quantum dephasing of a solid-state electron spin qubit in a large nuclear spin bath coupled by long-range hyperfine-mediated interactions, Phys. Rev. B **79**, 245314 (2009).

[45] A. Henstra, P. Dirksen, J. Schmidt, and W. Wenckebach, Nuclear spin orientation via electron spin locking (NOVEL), Journal of Magnetic Resonance (1969) **77**, 389 (1988).

[46] J. Hu, A. Urvoy, Z. Vendeiro, V. Crépel, W. Chen, and V. Vuletić, Creation of a Bose-condensed gas of ^{87}Rb by laser cooling, Science **358**, 1078 (2017).

[47] V. V. Dobrovitski, A. E. Feiguin, R. Hanson, and D. D. Awschalom, Decay of Rabi oscillations by dipolar-coupled dynamical spin environments, Phys. Rev. Lett. **102**, 237601 (2009).

[48] J. R. Petta, J. M. Taylor, A. C. Johnson, A. Yacoby, M. D. Lukin, C. M. Marcus, M. P. Hanson, and A. C. Gossard, Dynamic nuclear polarization with single electron spins, Phys. Rev. Lett. **100**, 067601 (2008).

[49] H. Christ, J. I. Cirac, and G. Giedke, Quantum description of nuclear spin cooling in a quantum dot, Phys. Rev. B **75**, 155324 (2007).

[50] G. Gillard, I. M. Griffiths, G. Ragunathan, A. Ulhaq, C. McEwan, E. Clarke, and E. A. Chekhovich, Fundamental limits of electron and nuclear spin qubit lifetimes in an isolated self-assembled quantum dot, Npj Quantum Inf. **7**, 43 (2021).

[51] E. A. Chekhovich, M. Hopkinson, M. S. Skolnick, and A. I. Tartakovskii, Suppression of nuclear spin bath fluctuations in self-assembled quantum dots induced by inhomogeneous strain, Nat. Commun. **6**, 6348 (2015).

[52] P. Millington-Hotze, H. E. Dyte, S. Manna, S. F. C. da Silva, A. Rastelli, and E. A. Chekhovich, Approaching a fully-polarized state of nuclear spins in a semiconductor quantum dot, arXiv:2302.05489 [cond-mat.mes-hall] (2023).

[53] T. Botzem, R. P. G. McNeil, J.-M. Mol, D. Schuh, D. Bougeard, and H. Bluhm, Quadrupolar and anisotropy effects on dephasing in two-electron spin qubits in GaAs, Nat. Commun. **7**, 11170 (2016).

[54] E. A. Chekhovich, S. F. C. da Silva, and A. Rastelli, Nuclear spin quantum register in an optically active semiconductor quantum dot, Nat. Nanotechnol. **15**, 999 (2020).

[55] N. Khaneja, T. Reiss, C. Kehlet, T. Schulte-Herbrüggen, and S. J. Glaser, Optimal control of coupled spin dynamics: Design of NMR pulse sequences by gradient ascent algorithms, J. Magn. Reson. **172**, 296 (2005).

[56] K. R. Brown, A. C. Wilson, Y. Colombe, C. Ospelkaus, A. M. Meier, E. Knill, D. Leibfried, and D. J. Wineland, Single-qubit-gate error below $\mathbf{10^{-4}}$ in a trapped ion, Phys. Rev. A **84**, 030303 (2011).

[57] N. Tomm, A. Javadi, N. O. Antoniadis, D. Najer, M. C. Löbl, A. R. Korsch, R. Schott, S. R. Valentin, A. D. Wieck, A. Ludwig, and R. J. Warburton, A bright and fast source of coherent single photons, Nat. Nanotechnol. **16**, 399 (2021).

[58] M. H. Appel, A. Tiranov, A. Javadi, M. C. Löbl, Y. Wang, S. Scholz, A. D. Wieck, A. Ludwig, R. J. Warburton, and P. Lodahl, Coherent spin-photon interface with waveguide induced cycling transitions, Phys. Rev. Lett. **126**, 013602 (2021).

[59] C. Barthel, D. J. Reilly, C. M. Marcus, M. P. Hanson, and A. C. Gossard, Rapid single-shot measurement of a singlet-triplet qubit, Phys. Rev. Lett. **103**, 160503 (2009).

[60] J. M. Kindem, A. Ruskuc, J. G. Bartholomew, J. Rochman, Y. Q. Huan, and A. Faraon, Control and single-shot readout of an ion embedded in a nanophotonic cavity, Nature **580**, 201 (2020).

[61] N. O. Antoniadis, M. R. Hogg, W. F. Stehl, A. Javadi, N. Tomm, R. Schott, S. R. Valentin, A. D. Wieck, A.

Ludwig, and R. J. Warburton, Cavity-enhanced single-shot readout of a quantum dot spin within 3 nanoseconds, arXiv:2210.13870 [quant-ph] (2022).

[62] E. V. Denning, D. A. Gangloff, M. Atatüre, J. Mørk, and C. Le Gall, Collective quantum memory activated by a driven central spin, Phys. Rev. Lett. **123**, 140502 (2019).

[63] G. Anikeeva, O. Marković, V. Borish, J. A. Hines, S. V. Rajagopal, E. S. Cooper, A. Periwal, A. Safavi-Naeini, E. J. Davis, and M. Schleier-Smith, Number partitioning with Grover's algorithm in central spin systems, PRX Quantum **2**, 020319 (2021).

[64] J. Johansson, P. Nation, and F. Nori, Qutip: An open-source python framework for the dynamics of open quantum systems, Comput. Phys. Commun. **183**, 1760 (2012).

[65] J. Johansson, P. Nation, and F. Nori, Qutip 2: A python framework for the dynamics of open quantum systems, Comput. Phys. Commun. **184**, 1234 (2013).

[66] L. Zhai, M. C. Löbl, G. N. Nguyen, J. Ritzmann, A. Javadi, C. Spinnler, A. D. Wieck, A. Ludwig, and R. J. Warburton, Low-noise GaAs quantum dots for quantum photonics, Nat. Commun. **11**, 4745 (2020).

[67] E. A. Chekhovich, I. M. Griffiths, M. S. Skolnick, H. Huang, S. F. C. da Silva, X. Yuan, and A. Rastelli, Cross calibration of deformation potentials and gradient-elastic tensors of GaAs using photoluminescence and nuclear magnetic resonance spectroscopy in GaAs/AlGaAs quantum dot structures, Phys. Rev. B **97**, 235311 (2018).

[68] F. K. Malinowski, F. Martins, L. Cywiński, M. S. Rudner, P. D. Nissen, S. Fallahi, G. C. Gardner, M. J. Manfra, C. M. Marcus, and F. Kuemmeth, Spectrum of the nuclear environment for GaAs spin qubits, Phys. Rev. Lett. **118**, 177702 (2017).

[69] M. Cerezo, A. Sone, T. Volkoff, L. Cincio, and P. J. Coles, Cost function dependent barren plateaus in shallow parametrized quantum circuits, Nat. Commun. **12**, 1791 (2021).